

Measurement of ${}^2\text{H}(\vec{\gamma}, p)n$ with linearly polarized photons in the Δ resonance region

G. Blanpied,⁴ M. Blecher,⁶ A. Caracappa,¹ C. Djalali,⁴ M.-A. Duval,⁴ G. Giordano,² K. Hicks,⁷ S. Hoblit,¹ M. Khandaker,¹⁰ O. C. Kistner,¹ G. Matone,² L. Miceli,^{1,4} W. K. Mize,⁴ C. Molinari,^{9,1} B. M. Preedom,⁴ A. M. Sandorfi,¹ C. Schaerf,³ R. M. Sealock,⁵ D. Rebreyend,⁸ C. E. Thorn,¹ S. T. Thornton,⁵ K. Viziri,¹¹ C. S. Whisnant,^{4,*} and X. Zhao⁶

(The LEGS Collaboration)

¹Physics Department, Brookhaven National Laboratory, Upton, New York 11973

²INFN-Laboratori Nazionali di Frascati, Frascati, Italy

³Università di Roma "Tor Vergata" and INFN-Sezione di Roma 2, Rome, Italy

⁴Department of Physics, University of South Carolina, Columbia, South Carolina 29208

⁵Department of Physics, University of Virginia, Charlottesville, Virginia 22901

⁶Physics Department, Virginia Polytechnic Institute and State University, Blacksburg, Virginia 24061

⁷Department of Physics, Ohio University, Athens, Ohio 45701

⁸Institut des Sciences Nucleaires, 53, av. des Martyrs, 38026 Grenoble Cedex, France

⁹Università di Genova and INFN-Sezione di Genova, 16146 Genova, Italy

¹⁰Department of Physics, Norfolk State University, Norfolk, Virginia 23504

¹¹Physics Department, Rensselaer Polytechnic Institute, Troy, New York 12180

(Received 23 July 1999; published 30 December 1999)

The photodisintegration of deuterium with linearly polarized light has been measured in the energy range of 110–315 MeV. The results of five independent measurements using three detector systems, two liquid target geometries, and two photon energy distribution end points are presented. These data are combined into one average data set with a systematic uncertainty of $\pm 5\%$. The statistical precision of this combined data set, coupled with the sensitivity to the strength of the short range tensor interaction observed in the parallel-perpendicular cross section difference, makes this an attractive reaction for investigating aspects of the NN interaction. To do this reliably requires a complete, systematic description of the reaction through the Δ region. Recent NN - $N\Delta$ coupled-channel calculations which include fully retarded pion potentials are compared with multipole fits to the data. These calculations cannot reproduce the energy and angle dependence of the data. The character of the disagreement suggests that the remaining problems may lie with the treatment of the Δ .

PACS number(s): 25.20.Dc, 21.30.Fe, 13.75.Cs

The simple spin structure of the deuteron wave function and the dominance of the $\gamma N\Delta$ coupling near $E_\gamma \sim 300$ MeV make the photodisintegration of deuterium particularly well suited for the study of the NN and the $N\Delta$ interactions. Nevertheless, the experimental difficulties encountered with photon beams have resulted in photodisintegration data with 10–15% uncertainties in the Δ region. This is readily seen in the integrated cross sections from several of the more recent experiments, as shown in Fig. 1. Knowledge of the beam polarization asymmetry is even less certain where there are fewer measurements available and these data have larger uncertainties. Although correlating the sparse beam asymmetry data with the unpolarized cross sections could help, prior to the work reported here, the two were never measured at the same time.

The absorption of a photon by a nucleon at these energies is predominantly *via* the magnetic dipole interaction, flipping the spin of one of the quarks, leading directly to an $N\Delta$ intermediate state. If this process occurs in the two-nucleon system, then pure $M1$ transitions in the *photon-nucleon* system will involve other multipoles in the *photon-deuteron* system. However, if this mixing is not too severe, then the interaction is dominantly $M1$ in both coordinate systems. In

the photon-deuteron system, $M1$ photon absorption produces a nucleon spin-flip rather than a quark spin-flip. Thus, a dominant portion of the interaction proceeds through an $N\Delta$ intermediate state and results in the spin flip of a nucleon. This coupling of the quark and nucleon spin-flip processes and the conservation of angular momentum, has important consequences. The wave function of the deuteron is primarily 3S_1 with a small additional 3D_1 component generated by the NN tensor force. The absorption of a $M1$ photon (photon-deuteron system) by a 3S_1 deuteron should produce a 1S_0 final state (nucleon spin flip) since the $\Delta l = 2$ $M1({}^3S_1) \rightarrow {}^1D_2$ transitions are strongly suppressed. However, requiring an $N\Delta$ intermediate state (quark spin flip) in this ${}^3S_1 \rightarrow {}^1S_0$ transition violates angular momentum conservation. Therefore, $M1$ Δ excitation proceeds mainly through the D state of the deuteron wave function via a $\Delta l = 0$ $M1({}^3D_1) \rightarrow {}^1D_2$ transition. This observation allows us to understand why the cross section at the peak of the Δ (≈ 260 MeV) is comparable to that seen at 100 MeV in Fig. 1. Well below the Δ where the quark/nucleon spin-flip processes are not strongly coupled, the reaction can proceed through the dominant S -wave component of the wave function and the cross sections are much larger. Thus, we see that requirement both of a quark and nucleon spin-flip intimately couples the reaction with the NN tensor interaction.

The tensor interaction is predominantly one pion exchange and the $NN\pi$ coupling constant essentially deter-

*Electronic address: whisnant@sc.edu

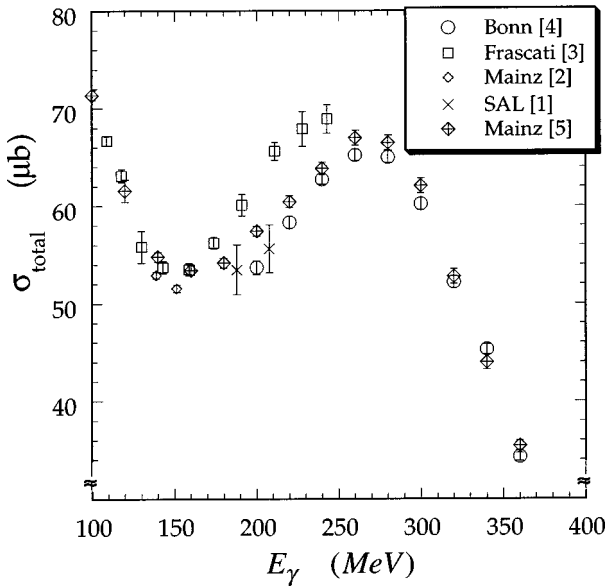


FIG. 1. Integrated cross section data for ${}^2\text{H}(\gamma,p)n$ taken with monochromatic photons in the region of the Δ resonance. The Saskatoon [1] data is represented by crosses, the Mainz (1989) [2] data is displayed as diamonds, the Frascati [3] data is shown with squares, the Bonn [4] data is shown with circles, and the Mainz (1996) data [5] is shown as the crossed diamonds.

mines the long-range character of the interaction (for example, the asymptotic D/S state ratio) but this does not fix the short-range properties of the tensor interaction. In principle, this short-range information can be obtained from phase-shift analyses of $n-p$ scattering by extracting the amplitude for the ${}^3S_1 \rightarrow {}^3D_1$ transition, ε_1 . However, the uncertainties associated with this procedure are large [6].

The photodisintegration of deuterium with linearly polarized light offers a new avenue for addressing this question. Polarization observables are sensitive to interference terms that illuminate effects that are not easily accessible through unpolarized cross section measurements. Recent calculations of the cross sections and beam-polarization asymmetries [7,8] confirm the arguments given above. In particular, the meson exchange (MEC) as well as delta-isobar (IC) currents strongly affect the asymmetry. Thus, this reaction offers a fertile testing ground for models of both the NN and $N\Delta$ interactions.

We describe here a series of experiments conducted at the Laser Electron Gamma Source (LEGS) located at the National Synchrotron Light Source (NSLS) at Brookhaven National Laboratory. Five independent measurements of the ${}^2\text{H}(\gamma,p)n$ reaction have been conducted (experiments $L1$ and $L3$) with linearly polarized photons. These experiments used three proton detector systems, two liquid deuterium targets, and two photon energy distribution end points produced with different laser wavelengths with their correspondingly different polarizations. Although highlights of this data have been presented before [9,10], full details are given here. These measurements provide the first simultaneous determination of cross sections and beam-polarization asymmetries. The data sets overlap in various kinematic regions between

110 and 315 MeV, and the agreement in the regions of overlap is excellent. From these data, a grand average data set is constructed by taking error weighted means of overlapping measurements. This “net” data set is available from the LEGS web page [11] and is tabulated here. In Sec. I, a summary of the experiments and a comparison to existing data is given. In Sec. II, we examine the sensitivity to the short range tensor component of the interaction by comparing the data with impulse approximation model calculations. This is extended in Sec. III by a comparison with coupled channel calculations.

I. THE LEGS EXPERIMENTS

For LEGS experiments $L1$ and $L3$, protons from the photodisintegration reaction were observed with three complementary detector systems: an array of phoswich scintillators, a NaI/Si-microstrip system (NSS), and a NaI wire chamber combination (NWC). Operating some in coincidence with the photon tag and some untagged permitted measurement of excitation functions from below pion threshold up to the highest energies then available. At the same time, complete angular distributions were also obtained throughout the tagged energy range.

During the $L1$ run period, data was collected with the tagged phoswich at seven angles simultaneously and the untagged NSS at three angles sequentially up to a maximum energy of 228 MeV. The $L3$ data collection was done in two periods. Tagged phoswich data covering eight angles and untagged NSS at two successive angles were used in $L3a$. During $L3b$, the tagged NWC system was positioned at $\sim 90^\circ$. For the $L3$ measurements, the maximum photon energy was 332 MeV.

A. Phoswich detector array

Proton angular distributions were measured with an array of 24 phoswich detectors placed in groups of three at seven laboratory angles (15° , 35° , 55° , 75° , 95° , 115° , 135°) with an eighth angle (155°) added for $L3$. Each detector covered a solid angle of $20.72 \text{ msr} \pm 3.1\%$. The detectors were arranged as shown in Fig. 2 with the reaction plane vertical. These scintillator “sandwiches” consist of 2 mm of $\text{CaF}_2(\text{Eu})$ followed by 38.1 cm of plastic (15° and 35°) or 1 mm CaF_2 in front of 26.0 cm plastic scintillator. Both scintillators are read out by the same phototube. This compact design takes advantage of the very different signal decay times in the two scintillator materials. (The decay constant for CaF_2 is $0.94 \mu\text{s}$.) A typical $\Delta E-E$ spectrum is shown in Fig. 3. By splitting the signal and integrating the fast and slow components separately as shown in the insert, separate E and ΔE information are obtained. An 80 ns wide gate was used to integrate the prompt plastic peak. After a 100 ns delay, a $1 \mu\text{s}$ gate was opened to integrate the slow ΔE signal. This readout method mixes the two signals resulting in nonorthogonal axes as seen in the figure. The unmixed data is recovered in the off-line analysis by applying a linear transformation to the raw data. Once unmixed, the data is energy calibrated and spectra from the three adjacent detec-

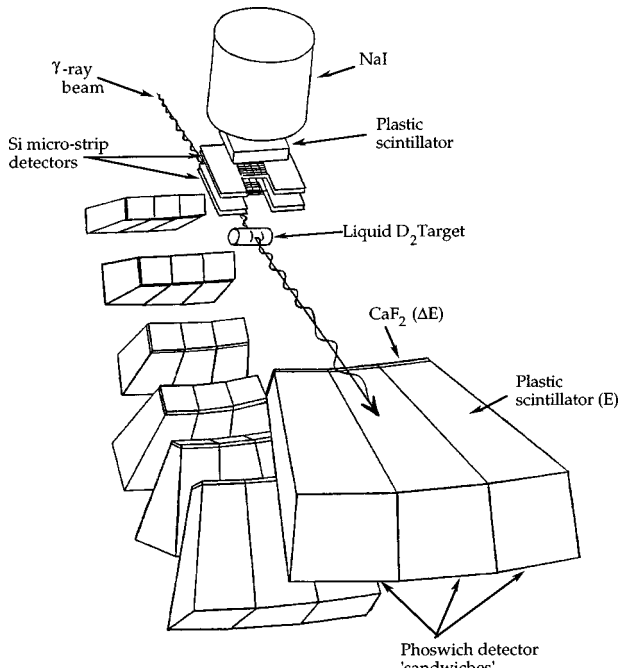


FIG. 2. The arrangement of the phoswich and NaI/Si-strip detector systems. The reaction plane is vertical.

tors combined, increasing the statistics and reducing the uncertainty in placing cuts to extract yields. Since we are observing a two-body final state, the kinematics are over determined by measuring the photon energy (tagging) and the proton angle and energy. All of this information is conveniently incorporated in the analysis by computing the missing mass. Protons from the photodisintegration reaction then appear as a peak at the mass of the neutron.

The resulting missing mass spectra at each angle were next corrected for accidental coincidences. The time between the photon tag and the proton signal was digitized as shown in Fig. 4. In this figure, the 18.9 ns bunch structure of the stored electron beam is clearly evident. By starting with a loose coincidence (80 ns) between a nuclear event and the

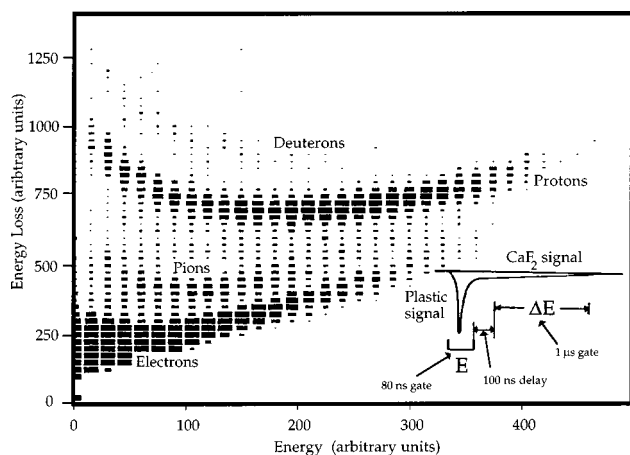


FIG. 3. A typical raw ΔE vs E spectrum obtained with a phoswich detector. The inset schematically shows the setting of the gates to recover both pieces of information from one phototube.

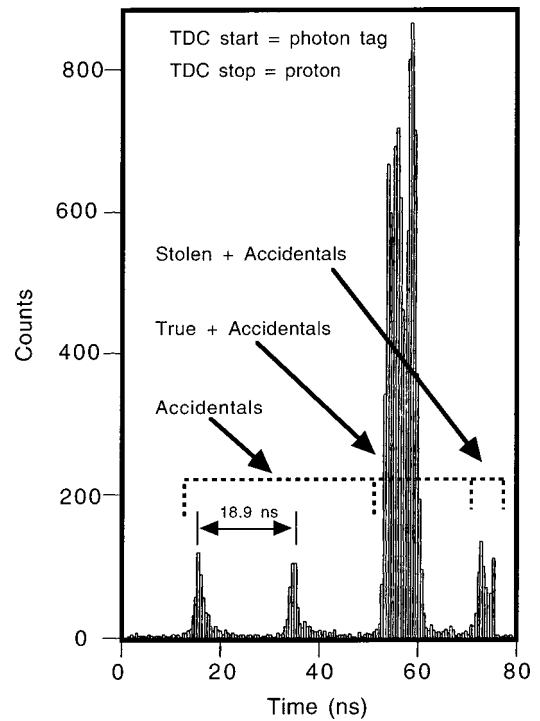


FIG. 4. A TDC spectrum showing the placement of true and accidental gates. Both preceding accidental buckets were included to improve statistics.

logical OR of all the photon tagging detectors (the tagger is described in Sec. ID 1) that had the timing of the tag at the nuclear rate, and stopping with the nuclear event, the accidental peaks preceding the true peak represent TDC starts generated by later tags. Thus, for a count to be entered into one of these peaks, the true tag must be missing. However, the accidental peak appearing at a later time than the true peak contains two classes of accidentals. Events in this peak come from earlier tags for which a true tag would have been missing (as with the later tags) and those for which a true tag would have been recorded had the electronics not been busy. Since one single-hit TDC per nuclear detector was used, these earlier TDC starts can thus remove events from the true peak. These *stolen* events simply scale the data. The accidentals correction (later tags, earlier TDC peaks) is done by producing spectra gated on the out-of-time tags immediately preceding the true peak and subtracting these from spectra gated on the true peak. This produces accidental corrected spectra for target full and target empty. From the difference of these spectra, the yields are extracted. The correction for the stolen events (earlier tag, later peak) is made to the extracted yields by the multiplicative factor, F_s ,

$$F_s = \frac{1}{1 - \frac{S-A}{T-A}}, \quad (1)$$

where T , S , and A are the number of counts in the true, stolen, and accidental peaks, respectively. Since this correction depends on both the photon tagging rate and the proton rate into a particular detector, a different correction was com-

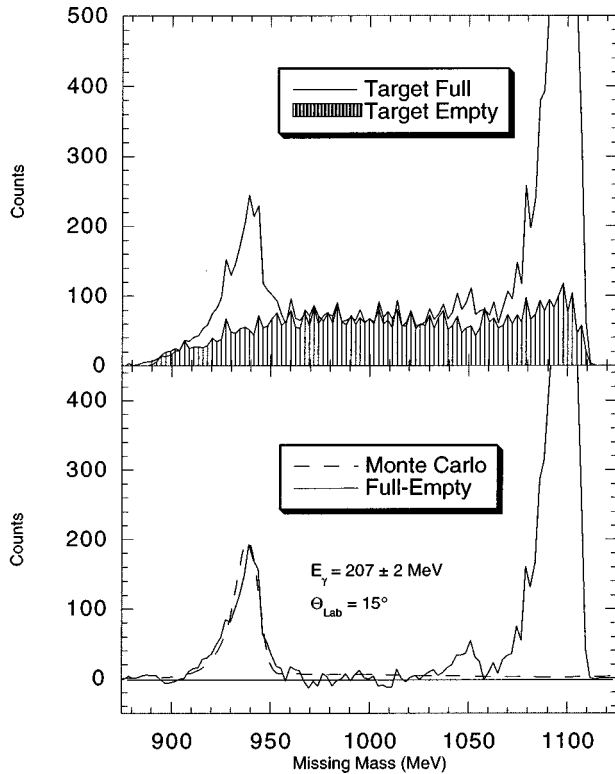


FIG. 5. The accidental corrected, target full (line) and target empty (filled) missing mass spectra computed from summed spectra from adjacent detectors at 15° are shown in the upper panel. These spectra correspond to the $E_\gamma = 207$ MeV tag. The lower panel shows the full-empty difference (solid) and the Monte Carlo calculation (dashed).

puted for each detector and photon polarization state (see Sec. ID 5). Typically, F_s was about 1.044 ± 0.001 .

To optimize the signal-to-noise ratio in the extracted yields, only the peaks were integrated. The losses from un-integrated tails are estimated with a Monte Carlo calculation using the CERN GEANT program. A comparison of these calculations with published peak-to-tail ratios found them to be within $\pm 1\%$ of published data [12,13,14].

The accidental corrected missing mass spectra corresponding to target full, target empty, the full-empty difference, and the GEANT calculation for the detectors at 15° are shown in Fig. 5 for the 207 MeV tag. The sharp rise at missing masses larger than 1070 MeV is from pion production. The over determination of the kinematics makes the separation of this reaction trivial. In the 15° and 75° spectra (Fig. 6 and Fig. 7) another small, broad peak is seen centered near 1050 MeV. This peak contains pions that are misidentified by the phoswich readout method. Muons from positive pions that stop in a phoswich detector will occasionally decay within the delayed ΔE gate. When this happens, the resulting 4.1 MeV deposited in the plastic adds to the wide gate ΔE signal, shifting the pion inside the proton distribution. As can be seen from Figs. 5–7, this misidentification is never a problem at any angle.

At the energies reported here, the protons associated with pion production have energies significantly above detector

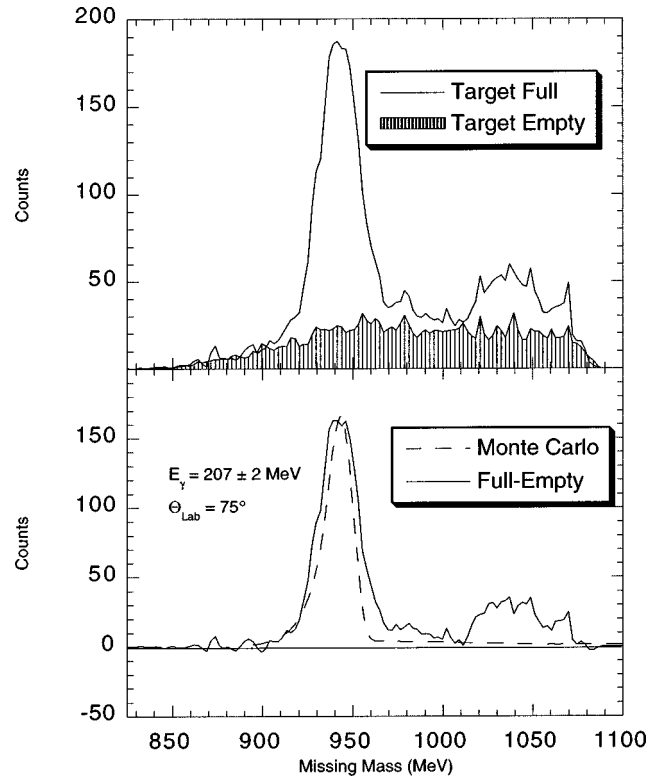


FIG. 6. The same as Fig. 5 for the detectors at 75° .

thresholds only at the most forward angles. Hence, the large pion peak is not seen at 75° (Fig. 6) and 135° (Fig. 7). It is possible that such contamination from pion production at forward angles was a source of confusion in some earlier

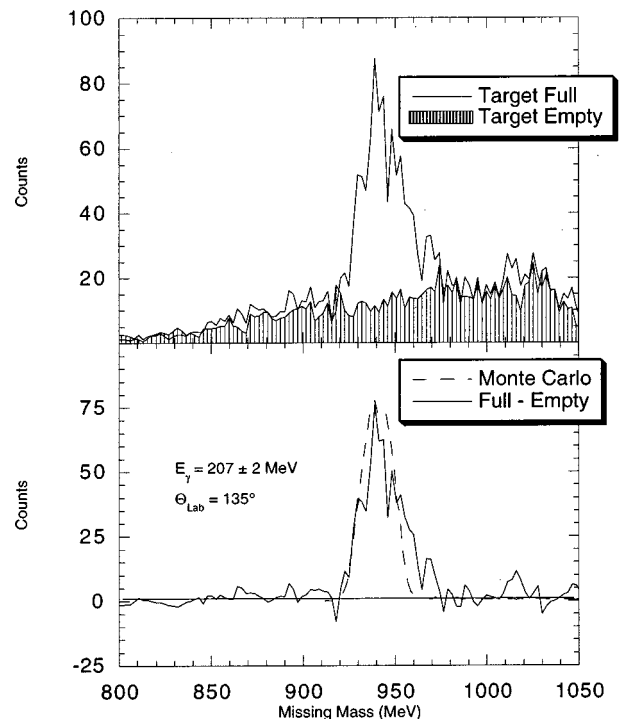


FIG. 7. The same as Fig. 5 for the detectors at 135° .

experiments and contributed to the large uncertainties above pion threshold. For example, the Frascati data shown in Fig. 1 were collected using a quasimonochromatic photon beam produced by positron annihilation in flight. This photon beam was accompanied by a significant bremsstrahlung tail which was included in the analysis. Although tests were made to insure that contamination was not a problem, all such published tests were made at 105° [15]. There is no indication that such tests were made at forward angles. We see in our spectra that there is little or no pion contamination at these larger angles because the associated protons are mostly below detection thresholds. The separation provided by over determination of the kinematics insures that this is not a problem in the present experiment.

B. NaI-silicon microstrip detector system (NSS)

A second detector system was used simultaneously with the phoswich array. This detector was operated untagged and relied on good angle resolution for accurate reconstruction of the photon energy. The azimuthal angle is measured by two planes of Si microstrips $42 \times 50 \text{ mm}^2$ in area and having 24 strips 2.0 mm apart providing $\approx 3^\circ$ resolution. The scattering angle is determined by two planes with an area of $40 \times 40 \text{ mm}^2$, each containing 200 strips, 0.2 mm apart and 0.3 mm thick. This gives an angular resolution in the reaction plane of $\approx 0.3^\circ$.

Behind the microstrips is a plastic trigger scintillator 1 cm thick and a 25.4 cm long \times 23.8 cm diameter NaI(Tl). These detectors provide ΔE and E signals for particle identification. A schematic of the NSS assembly is shown in Fig. 2. Data were collected with this detector located successively at 55° , 75° , and 91° .

Although photon tag information was collected with the NSS, it was not required in the trigger, permitting the data to be analyzed both tagged and untagged. The tagged data provided useful diagnostics to check for pion contamination and allow energy calibration of the NaI detector. This detector system has the unique ability in this experiment to extend the range of measurements well below the tagging and pion production threshold. Operating the detector untagged no longer overdetermines the kinematics and thus accurate energy and angular determination is required to compute the photon energy from the observed proton energy and angle.

The accurate angle reconstruction also provides an alternate method for eliminating the background from the target cell walls and vacuum windows. Projecting the observed proton trajectories back to the plane containing the beam axis allows the reconstruction of the target profile. Suitable cuts on this profile eliminated the contributions from the mylar target cell. Proton trajectories projected back to their intersection with a plane passing through the center of the target is shown in Fig. 8. The downstream vacuum window is seen to be well separated from the target. In Fig. 9, the projection onto a line passing through the center of the target is shown in the upper panel. Here, the target cut (dashed lines) is seen to completely eliminate the contributions of the walls. The lower panel shows the proton spectra obtained for the entire target and the portion that passed the target cut.

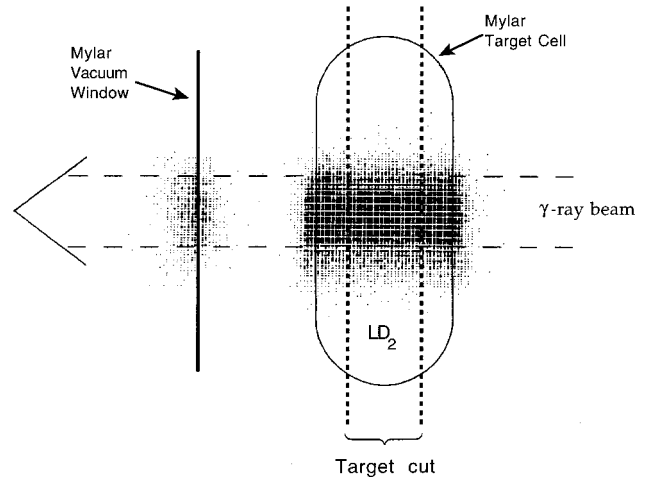


FIG. 8. The NSS data projected onto a plane passing through the center of the target. The downstream vacuum window is clearly seen. The location of the target cell walls and the target cut to eliminate their contribution is indicated.

Alternately, the microstrip data may be ignored and a full and empty target subtraction done as for the phoswich detectors. Both analysis methods were used on the 75° data and found to be in excellent agreement. Empty target data were collected only at 75° . At all other angles, target reconstruction was used to eliminate backgrounds.

The efficiency of the silicon microstrip planes was obtained directly from the data. For events identified as protons by their $E-\Delta E$, the efficiency is obtained from the fraction of events observed by a particular plane when the other three are required. The total efficiency of the four planes (the product of the four separate efficiencies) is 0.967 ± 0.028 . The efficiency of the NSS system for electrons is very low since electrons scatter through large angles in the silicon and are eliminated by the requirement of a straight track.

C. NaI-wire chamber detector system (NWC)

In a separate run (*L3b*), using the second target (described in Sec. I E) a third detector assembly was used. This system consisted of a set of four wire chambers, two x planes and two y planes, followed by a $3 \text{ mm} \times 30 \text{ cm}$ diameter and $2.5 \text{ cm} \times 60 \text{ cm}$ diameter plastic scintillators, and a $48.3 \text{ cm long} \times 48.3 \text{ cm diameter}$ NaI detector. Because the diameter of the plastic scintillator was larger than the NaI, the wire chambers were used to define the solid angle of the system and ensure that only events from the target were included in the analysis. The wire chamber efficiency was found in the same way as that of the silicon microstrips to be 0.982 ± 0.006 .

The NWC trigger required a photon tag and the detector was placed at a laboratory angle of 90° throughout the entire run. Fixing the large solid angle detector at one angle throughout the experiment produced data with high statistical precision.

After energy calibration of the plastic and NaI scintillators, the missing mass was computed producing spectra for

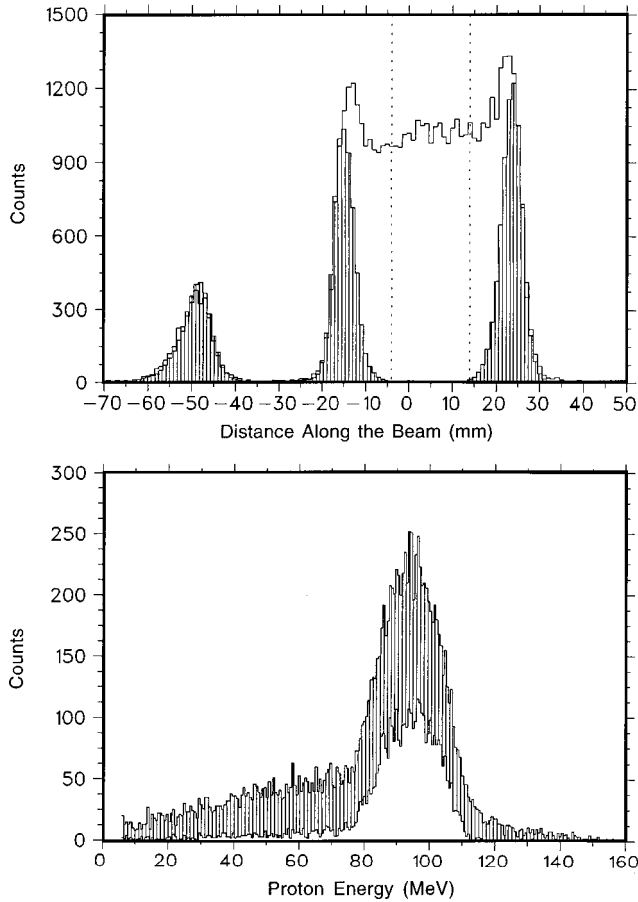


FIG. 9. The upper panel shows the target reconstruction using the NSS detector located at 75° . The horizontal axis is the position along the beam with downstream being negative. Superimposed on the target full data (line) is the flux normalized target empty data (filled). The two vertical dotted lines corresponding to those shown in Fig. 8 show the cut used to eliminate the background due to the target cell walls. The lower panel shows the proton spectrum for the full target (filled) and for those events that pass the target cut.

each photon energy bin from which the yields could be extracted. These spectra were corrected for accidental and stolen coincidences as was done for the phoswich detectors.

D. Photon beam

1. General characteristics

Linearly polarized γ -rays were produced by backscattering polarized laser light from the stored 2.54 GeV electron beam in the NSLS. The ring is operated at a frequency of 52.88 MHz with 25 out of 30 possible electron bunches filled. The resulting photon beam thus has bunches separated by 18.9 ns (see Fig. 4).

The backscattered photon energy, E_γ , is related to the laser and electron energies, ε and $E_e = \gamma m$, by

$$E_\gamma = \frac{4\varepsilon\gamma^2}{1 + 4\varepsilon\gamma/m + \vartheta\gamma^2}, \quad (2)$$

where m is the electron mass and $\pi - \vartheta$ is the photon scattering angle. Maximum γ -ray energies correspond to $\vartheta = 0^\circ$. This maximum γ -ray energy is called the *Compton edge*.

During the *L1* run period, an Ar-ion laser was operated at 488 nm producing the Compton edge at 228 MeV. The *L3* experiments were conducted with the laser operated in a multiline mode, emitting three lines at 364, 351, and 333 nm. This produces a spectrum that is the superposition of three spectra with Compton edges at 297, 307, and 321 MeV, respectively. Just prior to experiment *L3b*, the ring energy was increased to 2.58 GeV. Backscattering with the multiline UV produced Compton edges at 307, 317, and 332 MeV.

The physical process is simply Compton scattering in the rest frame of the electron and the tremendous amplification in scattered photon energy arises from a Lorentz boost to the electron rest frame and a second boost back to laboratory frame. The laser photon energy increases when transforming from the lab to the electron rest frame. The scattering of this boosted photon is described by the Klein-Nishina scattering of light from a free electron. After the scattering, the boost back to the laboratory produces a photon *beam* by collapsing the entire angular distribution into a narrow cone about the electron beam [16]. The spatial distribution of the photon beam produced by backscattering 488 nm laser light as observed after the nuclear target (~ 40 m from the center of the interaction region) is shown in Fig. 10. The upper panel shows the beam profile for an energy near the maximum. The horizontal ellipse reflects the divergence of the stored electron beam which is $80 \mu\text{rad}$ vertically and $240 \mu\text{rad}$ horizontally. Nickel slits, located 20 m upstream of the target, immediately followed by a magnet to remove e^\pm pairs, are used to insure that the photon beam is completely confined within the target. As the photon energy decreases from the maximum, the beam spot develops a double-lobed structure as seen in Fig. 10. This is a result of the convolution of the beam divergence and the angular dependence of the Klein-Nishina cross section.

The γ -ray energies were determined to ~ 5.4 MeV, full width at half maximum (FWHM) by detecting the scattered electrons in a tagging spectrometer [17]. This resolution is dominated by the momentum spread of the electrons in the storage ring. By placing a large NaI detector directly in the beam and operating at low flux, the photon spectrum is observed, as is shown for the 488 nm laser line in Fig. 11. The upper panel shows an untagged spectrum with a lower limit determined only by the threshold of the detector. The center panel shows the spectrum obtained in coincidence with the 205 MeV tag and the bottom panel shows a 110 MeV tagged spectrum.

Also seen in the upper panel of Fig. 11 is a very small ($<1\%$) background extending above the Compton edge. This is bremsstrahlung produced by the resident gas in the synchrotron. The presence of this unpolarized component of the beam increases the flux but decreases the polarization. The correction to the polarization is discussed in Sec. ID 5.

The tagging focal plane contained two rows of $643.2 \text{ mm} \times 3.2 \text{ mm}$ scintillators offset from one another by 1.6 mm. For the *L1* experiments, the lower tagging limit was 185 MeV. For *L3*, the lower limit was 203 MeV. Other,

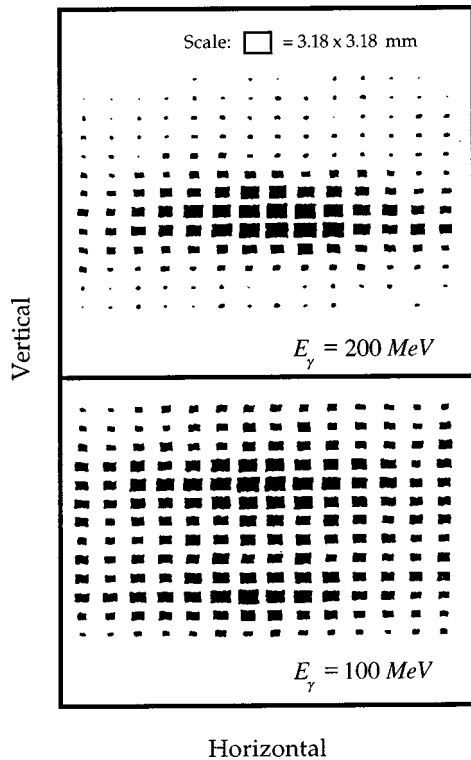


FIG. 10. The profile of the backscattered photon beam after passing through the nuclear target. The upper panel shows the distribution observed with two sets of crossed scintillators 3.18 mm wide. Thus each pixel in the diagram represents a 3.18×3.18 mm area. The sizes of the boxes are proportional to the intensity at each pixel. The upper panel shows the beam profile at 200 MeV, near the maximum energy of 235 MeV. The lower panel shows the double-lobbed beam profile at 100 MeV for horizontal polarization.

lower energy (and lower resolution) diagnostic tags were obtained by placing scintillators along the storage ring beam line.

2. Beam monitoring

In all experiments, the photon flux was measured with a sampling plastic scintillator/converter sandwich placed downstream of the target. The upstream scintillator served as a veto of e^+e^- pairs produced in the target and in air. This scintillator was followed by a Cu or Al converter representing $\approx 5\%$ of a radiation length. Following the converter was a second scintillator to count the number of e^+e^- pairs produced in the converter.

The monitor signal in coincidence with the tag was scaled. The accidental coincidences were measured by scaling a coincidence between the monitor signal and an out-of-time photon bunch, vetoed by the true coincidences. The veto insured that uncorrelated coincidences are counted just as in a single-hit TDC spectrum. The accidental corrected flux monitor is just the difference between the true and vetoed accidental scalers.

3. Monitor calibration

Calibration of the beam monitor was done at frequent intervals by comparing the monitor count rate to that ob-

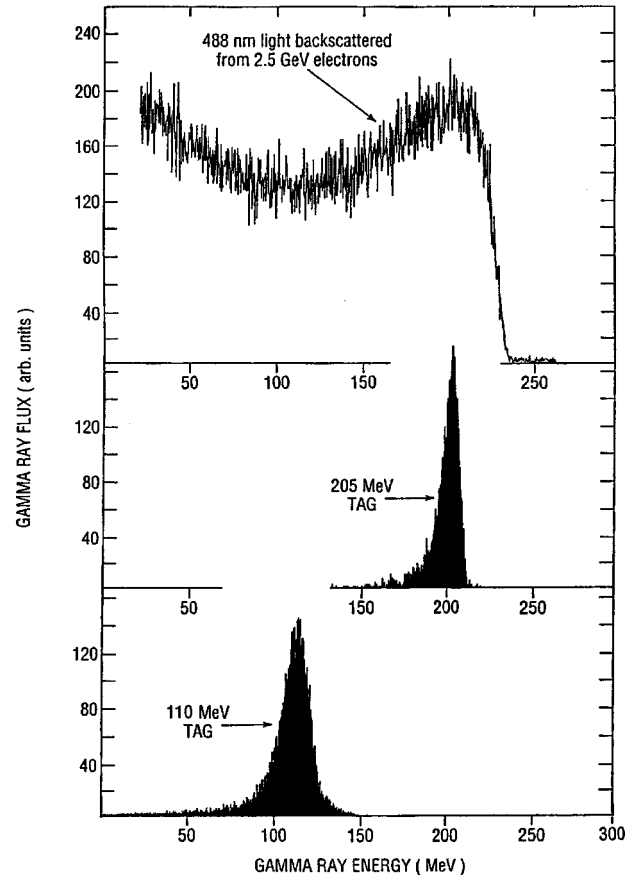


FIG. 11. The photon spectrum as observed by placing a large NaI detector directly in the beam at low flux. The top panel shows the spectrum from the Compton edge down to the detector threshold. The middle panel shows the NaI spectrum observed in coincidence with the 205 MeV tag. The bottom panel shows the spectrum seen in coincidence with a 110 MeV tag.

tained in a large ($23.8 \text{ cm} \times 35.6 \text{ cm}$) NaI detector placed directly in the beam. The flux was reduced to between 15 and 50 kHz to avoid pileup in the NaI by closing the slits to produce a beam spot size of approximately 4.5×4.5 mm.

In addition to lowering the flux by closing the slits as was done during a data run, other methods were investigated. Lower flux was also produced by reducing the laser power with the slits in the normal position. Reducing the electron beam current in the storage ring permitted calibration with full laser power and normally open slits. All of these methods were used for photon beams of both polarizations. No dependence on the electron current, laser power, slit opening, or polarization was observed. To insure the stability of the monitor at full flux and eliminate any rate dependence, phototubes were chosen which gave baseline-to-baseline pulse widths smaller than the time between successive beam bunches (18.9 ns) and the gains were monitored during each run.

4. Monitor data reduction

Monitor efficiencies were measured as a function of photon energy. A smooth energy dependence was fit to the data.

Rather than quote the normalization uncertainty as the error in this fit, the uncertainty is assumed to be the standard deviation of the data about the fit. In this way, any remaining nonstatistical fluctuations in the data were included in the quoted uncertainties.

The flux in each analysis bin for each run in experiment *L1* is found from a histogram of the tagger obtained by randomly sampling the tagger distribution. Because the tagged photons are limited to a small energy region near the maximum energy, this sample is indistinguishable from the true spectrum of photons on target as measured at the end of the run. These sample histograms are corrected for the monitor efficiency and normalized to give the correct integrated flux.

During *L3*, where the tagged energy range is much larger, the tagger spectrum in coincidence with the monitor was sampled directly. This allowed a bin-by-bin monitor efficiency correction giving a measure of the photon spectrum on target. At energies where *L1* and *L3* overlap, the two normalization methods were found to be in good agreement.

5. Photon polarization

The photon polarization was flipped between states with linear polarization parallel and perpendicular to the reaction plane at intervals randomly distributed between approximately 30 and 90 s. Due to a slight polarization dependence in the reflectance of the laser optics, the fluxes for the two polarization states are somewhat different. To reduce the differences in statistical uncertainties due to different fluxes, the average times spent in each polarization state were adjusted to give the same total flux on target.

The polarization of the backscattered photons is given by the Klein-Nishina [18] formula for the Compton scattering cross section and is substantially higher than that obtained from coherent bremsstrahlung. The polarization of the LEGS beam is found by using a Monte Carlo calculation to fold the Compton cross section with the electron and laser beam profiles and divergences. This results in a universal curve that gives the polarization as a function of the fraction of the end point energy.

As the photon energy decreases from the Compton edge, the laboratory scattering angle increases. Thus, lower energy photons scatter into larger annular regions. The azimuthal scattering angle dependence of the Compton cross section peaks in the plane perpendicular to the plane of the photon polarization. Folding the kinematics and the cross section produces a beam which displays a single, central spot for energies near the Compton edge but which splits into two spots as the photon energy decreases. Finally, the divergence of the electron beam dominates that of the laser and produces a beam profile elongated horizontally. This smears the beams spot into a horizontal lobe as shown in the upper panel of Fig. 10. The two-lobed nature of the horizontally polarized beam at energies below the maximum is seen in the lower panel. For vertical polarization below the Compton edge, the two horizontally smeared beam spots are in the horizontal plane. The long axes of the two lobes now align and they merge to produce a single, wider beam spot. Thus, photon beam has both an energy and polarization dependent profile.

In general, the photon polarization, \wp , is a function of both ϑ and φ . Since the photon energy divided by the maximum photon energy, $(E_\gamma/E_\gamma^{\max})$, and the scattering angle, ϑ , have a one-to-one relationship, it is convenient to express the polarization as $\wp(E_\gamma/E_\gamma^{\max}, \varphi)$. By integrating over the beam spot as cut by the Ni slits, the φ dependence is removed, leaving the polarization simply a function of energy.

Since the bremsstrahlung produced by the residual gas in the storage ring contributes to the flux but not to the polarization, the bremsstrahlung flux must be measured and the polarization corrected. Monitor event data are also collected with the laser shutter closed to obtain the shape of the bremsstrahlung spectrum and the bremsstrahlung flux. The unpolarized contribution was monitored throughout the experiments and was always a small ($< 1\%$) fraction of the flux, F_b , independent of energy within the tagging interval. The multiplicative correction to the polarization is $P_B = 1 - F_b$.

The laser polarization was measured after the laser-electron interaction region at the exit of a bending-magnet port upstream of the storage-ring straight section. This included the effect of any depolarization of the laser light in passing through optics damaged by the exposure to the synchrotron radiation.

For the phoswich data, where the reaction plane for each event was only determined to within the $\Delta\phi$ of the detectors placed at each angle, an angle dependent polarization correction is required. Because the polarization dependence enters the cross section multiplied by $\cos(2\phi)$ and the detectors cover a finite ϕ range, the polarization must be averaged over the face of the detectors. This introduces a multiplicative correction of

$$\Lambda(\theta) = \frac{1}{\Delta\phi} \int \cos(2\phi) d\phi. \quad (3)$$

For the NSS and NWC data, where the θ and ϕ of each event was known, this correction is unity.

The laser light was prepared in two states: perpendicular to the reaction plane, state 1, and parallel, state 2. Denoting the laser polarizations as measured after the storage-ring straight section, by P_1^l and P_2^l , the corresponding *net* γ -ray polarizations are given by

$$P_1^\gamma = \Lambda(\theta) P_B \left\{ P_1^l \wp_1(E_\gamma) - \frac{1}{2} (1 - P_1^l) [\wp_2(E_\gamma) - \wp_1(E_\gamma)] \right\}, \quad (4)$$

$$P_2^\gamma = \Lambda(\theta) P_B \left\{ P_2^l \wp_2(E_\gamma) - \frac{1}{2} (1 - P_2^l) [\wp_1(E_\gamma) - \wp_2(E_\gamma)] \right\}, \quad (5)$$

where $\wp_1(E_\gamma)$ and $\wp_2(E_\gamma)$ are the horizontal and vertical polarizations produced by backscattering a completely polarized laser beam from the stored electron beam. The second term in each equation arises from the decomposition of the light into its orthogonal components. Since $\wp_1 \approx \wp_2$, except at the lowest energies, this term is small. Figure 12 shows the resultant polarization for the *L3* run with $\Lambda(\theta) = 1$. The maximum value near $E_\gamma/E_\gamma^{\max} = 1$ indicates the degree of la-

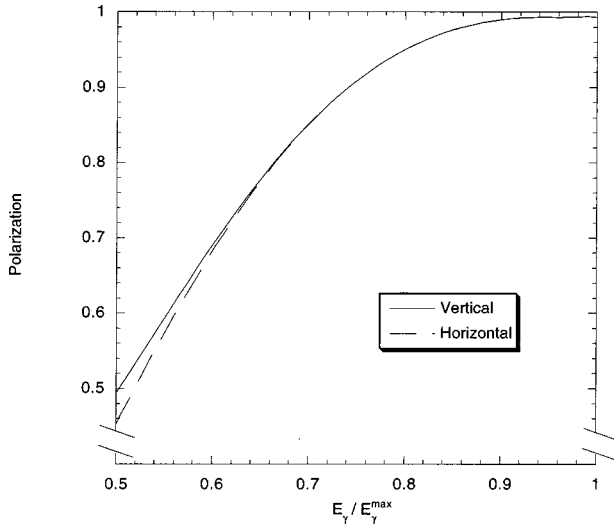


FIG. 12. The γ -ray polarization as a function of the fraction of the maximum energy with $\Lambda(\theta)=1$. This is the polarization obtained with the Ni slits set to the run conditions. The polarization dependence results from the change in the beam spot for energies below the maximum as seen in Fig. 10. Note the suppressed zero on the polarization axis.

ser polarization and the shape of the curve in this region reflects the fact that the laser was operated in a multiline mode for this run.

E. Targets

Two different liquid deuterium targets were used to collect data. The target used for all phoswich and NSS detector runs was a mylar cylinder 3.8 cm in diameter placed with the long axis perpendicular to the beam direction and in the horizontal plane. By choosing a vertical reaction plane, this presented an approximately uniform target thickness to the emerging protons at all angles. The walls of the cell were 1.3 mm thick. The upstream end of the vacuum vessel was a mylar window not viewed by the detectors. Background from the downstream mylar window contributed to the spectra observed with the phoswich detectors but not to the target reconstructions of the NSS system. The target thickness for the NSS analysis is determined directly from the target cut placed on the reconstruction shown in the upper panel of Fig. 9. For the phoswich detectors, the target thickness was determined by convoluting the beam profile with the target geometry. This introduces an energy dependence since the beam profile varies with energy. The effective target thickness calculated for the two polarizations is shown in Fig. 13.

The target used with the NWC was a cylinder with the long axis parallel to the beam direction. It was 13 cm long and 6 cm in diameter. The cell walls were 1.3 mm thick.

F. Observables and uncertainties

With photon polarization parallel and perpendicular to the reaction plane, two independent observables can be constructed. Which two are the most useful depends on the physics of interest. The general angular dependence of the cross section can be written as

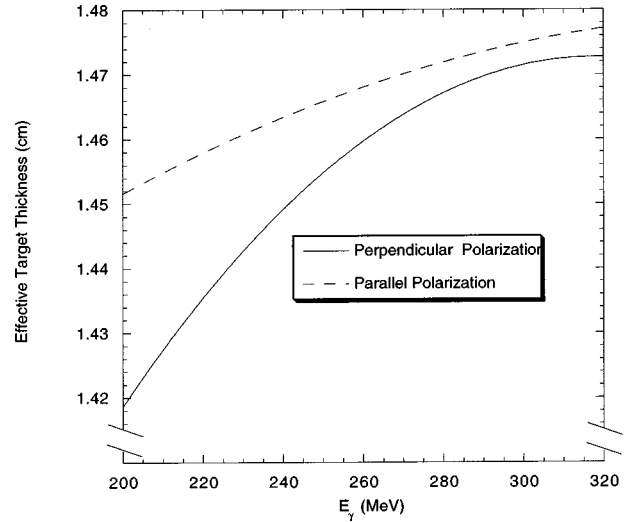


FIG. 13. The target thickness used for generating cross sections with the phoswich data. This thickness is the convolution of the energy and polarization dependent beam profile with the geometrical thickness of the target. This target thickness shown is for the $L3$ data run.

$$\frac{d\sigma}{d\Omega}(\theta, \phi) = \frac{d\sigma}{d\Omega}(\theta) + \hat{\Sigma}(\theta) \cos(2\phi), \quad (6)$$

where the cross sections are what would be observed with 100% polarized beam. In terms of these polarization corrected cross sections, the polarization-independent and dependent cross section are given by

$$\frac{d\sigma}{d\Omega}(\theta) = \frac{1}{2} \left(\frac{d\sigma_{\parallel}}{d\Omega} + \frac{d\sigma_{\perp}}{d\Omega} \right), \quad \hat{\Sigma}(\theta) = \frac{1}{2} \left(\frac{d\sigma_{\parallel}}{d\Omega} - \frac{d\sigma_{\perp}}{d\Omega} \right). \quad (7)$$

Because of experimental limitations, it has been customary to present the beam asymmetry, $\Sigma(\theta) = \hat{\Sigma}(\theta)/(d\sigma(\theta)/d\Omega)$ rather than the polarization-dependent cross section.

The polarization corrected cross sections, $d\sigma_{\parallel}(\theta)/d\Omega$ and $d\sigma_{\perp}(\theta)/d\Omega$, are related to those observed in polarization state 1 and state 2, by

$$\frac{d\sigma_{\parallel}}{d\Omega}(\theta) = \frac{1}{P_1^{\gamma} + P_2^{\gamma}} \left\{ (1 + P_2^{\gamma}) \frac{d\sigma_1}{d\Omega}(\theta) - (1 - P_1^{\gamma}) \frac{d\sigma_2}{d\Omega}(\theta) \right\} \quad (8)$$

and

$$\frac{d\sigma_{\perp}}{d\Omega}(\theta) = \frac{1}{P_1^{\gamma} + P_2^{\gamma}} \times \left\{ -(1 - P_2^{\gamma}) \frac{d\sigma_1}{d\Omega}(\theta) + (1 + P_1^{\gamma}) \frac{d\sigma_2}{d\Omega}(\theta) \right\}. \quad (9)$$

Thus, in terms of measured quantities, the unpolarized cross section is

$$\frac{d\sigma}{d\Omega}(\theta) = \frac{1}{P_1^\gamma + P_2^\gamma} \left[P_2^\gamma \frac{d\sigma_1}{d\Omega}(\theta) + P_1^\gamma \frac{d\sigma_2}{d\Omega}(\theta) \right], \quad (10)$$

the beam asymmetry is

$$\Sigma(\theta) = \frac{\frac{d\sigma_1}{d\Omega}(\theta) - \frac{d\sigma_2}{d\Omega}(\theta)}{P_2^\gamma \frac{d\sigma_1}{d\Omega}(\theta) + P_1^\gamma \frac{d\sigma_2}{d\Omega}(\theta)}, \quad (11)$$

and the polarization-dependent cross section (the numerator of the asymmetry) is

$$\hat{\Sigma}(\theta) = \frac{1}{P_1^\gamma + P_2^\gamma} \left[\frac{d\sigma_1}{d\Omega}(\theta) - \frac{d\sigma_2}{d\Omega}(\theta) \right]. \quad (12)$$

Since the photon has only two quantum states and the target is unpolarized, any two of $d\sigma_{\parallel}(\theta)/d\Omega$, $d\sigma_{\perp}(\theta)/d\Omega$, $d\sigma(\theta)/d\Omega$, $\Sigma(\theta)$, and $\hat{\Sigma}(\theta)$ completely characterize the reaction. Regardless of which observables are chosen, it is important to compute them directly from the experimental quantities $d\sigma_1/d\Omega$ and $d\sigma_2/d\Omega$ to correctly propagate the uncertainties.

The uncertainties in the data can be divided into three categories: statistical, polarization-dependent systematic, and polarization-independent systematic. Since the polarization-dependent systematic uncertainties cannot be factored out, they are combined in quadrature with the statistical uncertainties. The contributions to each of these are each described here.

Polarization. Because the sum of the polarizations enters only as an overall scale factor, the uncertainty in this sum contributes to the polarization-independent uncertainty. The polarizations also enter the expression for the unpolarized cross section in a way that does not factor out. The uncertainties in these quantities obviously contribute to the polarization-dependent systematic uncertainties.

TABLE I. The contributions to the systematic uncertainties for the two experiments *L1* and *L3*. Values listed are in percent and the totals are the sums in quadrature. The *L1/L3* total is the $\pm 1\sigma$ systematic uncertainty ascribed to the grand average data set.

Source	Experiment		
	<i>L1</i>	<i>L3</i>	
Target thickness	1.4	1.4	
Solid angle (phoswich)	3.1	3.1	
Background subtraction	0.4	0.4	
Photon flux	3.3	2.0	
Beam polarization (for each polarization state)	1.3	1.0	
GEANT efficiency (multiple scattering and reactions)	1.0	1.0	<i>L1/L3</i> Total
Total	5.0	4.2	5.0

Target thickness, solid angle, flux and Monte Carlo peak-to-tail ratios. The uncertainty in these quantities contribute only to the polarization-independent systematic uncertainty.

Background subtraction. For the data sets where a background subtraction was made (as opposed to reconstruction), there was a contribution to both the statistical and polarization-independent systematic uncertainties. Because the target-full and target-empty data runs were not taken at the same time, small off-line gain changes in the phoswich detectors were made. The uncertainty in this gain-matching procedure contributed to the systematic uncertainty.

The systematic uncertainties for these experiments are summarized in Table I.

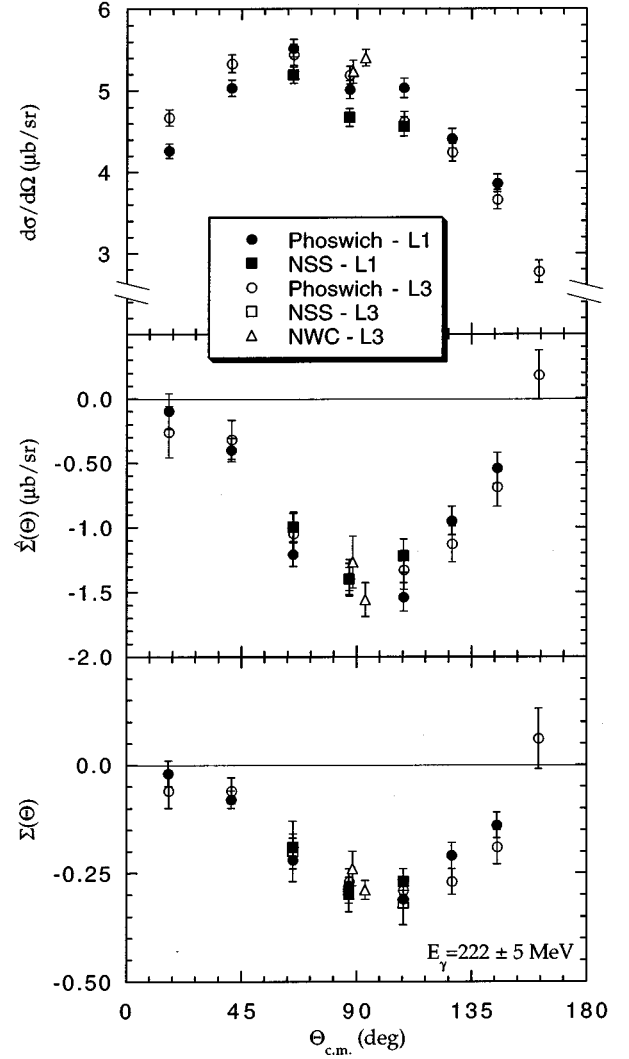


FIG. 14. Comparison of the five data sets obtained in experiments *L1* and *L3* at 222 MeV. The phoswich data from the lower energy data set are shown with filled circles, the lower energy NSS data are shown with filled squares, the phoswich data from the higher energy data set are shown with open circles, the higher energy NSS data are shown with open squares, and the NWC data are shown with open triangles. Only statistical and polarization-dependent uncertainties are shown. The top panel shows the unpolarized cross section, the middle contains the polarization dependent cross section, and the bottom shows the beam asymmetry.

G. Results

There are significant regions where the five data sets overlap and good agreement is obtained. The quality of this agreement is shown at 222 MeV in Fig. 14. Although there are small variations among the different data sets, these are within the expected systematic uncertainties of Table I. The excellent agreement of the asymmetries supports the consistency of the beam polarization calculations. The photon energy of 222 MeV is $0.94E_\gamma^{\text{max}}$ in the *L1* experiments and is $\approx 0.70E_\gamma^{\text{max}}$ in the *L3* experiments resulting in photon polarizations of 0.99 and 0.84, respectively. The agreement among the various data sets suggests that there are no significant systematic differences and that the data may be combined into one grand average set.

Data from these experiments span the energy range from 105 MeV to 317 MeV with different energy bin sizes and centroids for different detector sets. The data have been combined by dividing the energy range into 22 bins and averaging the data in each bin. The bins were chosen so that as many data sets as possible contributed to each. To choose these bins we look at $\Sigma(\theta_{\text{lab}}=75^\circ)$ because data for this observable at this angle is available from all measurements. The data binning is shown in Fig. 15.

Operating the NSS detector system untagged makes elimination of pion contamination more difficult at the higher energies. Even though the cross checks with the tagged subset of the NSS data indicate that this is not a problem in any of the data, we report absolute cross sections and asymmetries from the *L1* run but only asymmetries from the *L3* run to remove any possibility that the absolute cross sections are contaminated.

Data below the tagging threshold of 185 MeV come only from silicon strip detectors. In this region E_γ is available only indirectly via proton angle measurement and the reso-

lution turned out to be less than that obtained by tagging. Thus, the energy bin size is larger below tagging threshold. Once the energy bins are established, the centroid of each bin and the bin size are computed. There are two cases.

(1) To calculate the energy bin centroids for the excitation function at a given angle, only the data points from that particular angle will contribute to the centroid (and bin size) calculation.

(2) If the energy bin centroid for the angular distribution is to be calculated, then the data points from all the angles involved in the angular distribution are used.

For both cases, the bin averages weighted by the statistical and polarization-dependent systematic uncertainties were constructed. The energy bin centroids obtained by the two methods are somewhat different since more data is included in the computation of the centroid for the angular distributions than for the excitation functions. Because of the differing angular coverage, energy binning, and observables available for each detector, not every final energy bin is populated with all observables at all angles. The angular distributions are tabulated in Table II and plotted in Figs. 16–19 along with other published data. The excitation functions are presented in Table III and are plotted in Fig. 20 for the angles at which NSS data extends the data below the tagging threshold.

The size of the relative polarization-independent systematic errors may be assessed by computing the reduced χ^2 of all five data sets compared to the average. This gives $\chi^2/N_f = 277.8/92 = 3.0$ for the polarization-independent and dependent cross sections. For the asymmetries, where the polarization-independent uncertainties should not contribute, $\chi^2/N_f = 82.1/94 = 0.9$. Thus, we find a reduced χ^2 consistent with the cancellation of small scale errors in the asymmetry and their effect on the absolute cross sections is minor. Es-

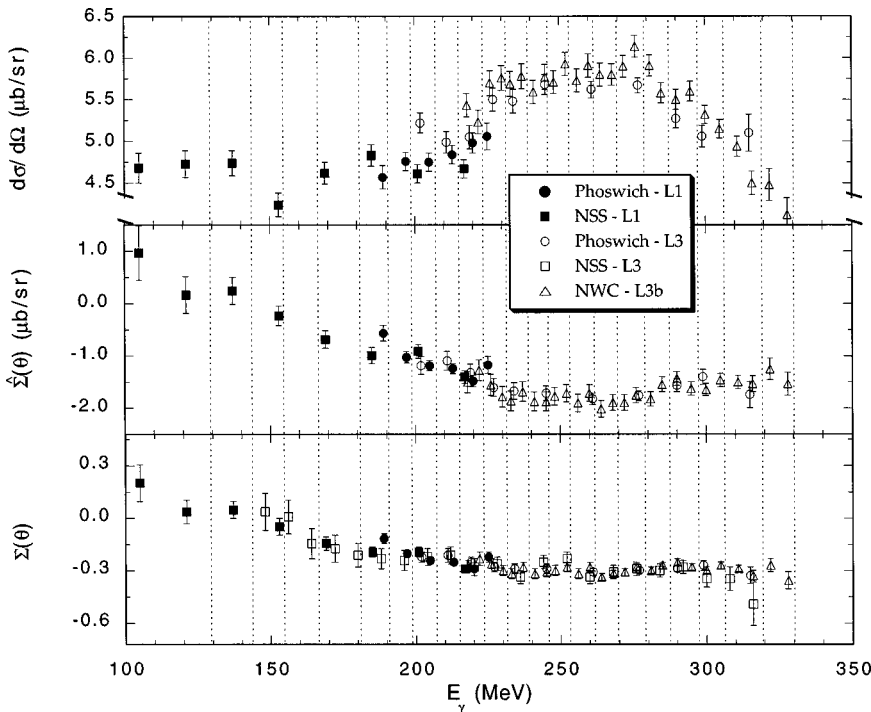


FIG. 15. The unpolarized and polarization dependent cross sections and the beam polarization asymmetry, at $\theta_{\text{lab}}=75^\circ$, as a function of energy for all data sets. The symbols for the data sets are the same as in Fig. 14. The dotted vertical lines indicate the binning used for producing the combined average data set.

TABLE II. Error weighted average angular distributions produced from the data obtained experiments *L1* and *L3*.

E (MeV)	$\theta_{c.m.}$ (deg)	$\frac{d\sigma}{d\Omega}(\theta)$ ($\mu\text{b/sr}$)	$\hat{\Sigma}(\theta)$ ($\mu\text{b/sr}$)	$\Sigma(\theta)$
187.5±5.4	16.3	3.24±0.13	0.22±0.24	0.07±0.07
	40.5	4.20±0.13	-0.09±0.15	-0.02±0.04
	64.3	4.90±0.09	-0.52±0.11	-0.11±0.02
	86.0	4.71±0.10	-0.78±0.11	-0.17±0.02
	107.3	4.18±0.10	-1.14±0.11	-0.26±0.03
	126.4	4.04±0.14	-0.65±0.16	-0.16±0.04
	144.2	2.85±0.14	-0.63±0.16	-0.22±0.06
	196.9±4.0	16.4	3.84±0.09	-0.02±0.16
40.6		4.40±0.10	-0.14±0.10	-0.03±0.02
64.5		4.96±0.11	-0.58±0.11	-0.11±0.02
86.3		4.76±0.11	-1.02±0.11	-0.21±0.02
107.6		4.28±0.11	-1.10±0.11	-0.27±0.03
126.6		3.72±0.11	-0.69±0.11	-0.18±0.03
144.4		3.36±0.11	-0.61±0.12	-0.18±0.04
203.5±5.0		16.5	3.82±0.07	0.12±0.13
	40.8	4.81±0.08	-0.30±0.09	-0.06±0.02
	64.8	5.14±0.07	-0.82±0.07	-0.16±0.01
	86.6	4.84±0.07	-1.10±0.07	-0.23±0.01
	107.9	4.57±0.07	-1.26±0.08	-0.28±0.02
	126.9	3.98±0.08	-0.81±0.10	-0.19±0.02
	144.6	3.28±0.08	-0.49±0.10	-0.15±0.03
	161.0	2.38±0.16	0.29±0.25	0.12±0.10
212.5±4.1	16.5	4.02±0.07	0.06±0.13	0.02±0.03
	41.0	4.96±0.08	-0.57±0.09	-0.11±0.02
	65.1	5.24±0.09	-0.97±0.09	-0.18±0.02
	86.9	4.90±0.08	-1.21±0.09	-0.25±0.02
	108.2	4.63±0.09	-1.27±0.09	-0.29±0.02
	127.2	4.27±0.09	-0.74±0.10	-0.17±0.02
	144.8	3.57±0.09	-0.56±0.10	-0.15±0.03
	161.2	2.52±0.17	-0.22±0.25	-0.09±0.10
219.3±4.8	16.6	4.38±0.08	-0.26±0.14	-0.06±0.03
	41.1	5.08±0.08	-0.34±0.09	-0.07±0.02
	65.2	5.33±0.07	-1.06±0.07	-0.20±0.01
	87.0	5.12±0.05	-1.43±0.06	-0.29±0.01
	108.3	4.70±0.08	-1.37±0.08	-0.29±0.02
	127.3	4.25±0.10	-0.99±0.11	-0.24±0.02
	144.9	3.73±0.10	-0.54±0.11	-0.14±0.03
	161.2	2.71±0.17	0.34±0.24	0.13±0.09
226.5±3.4	16.6	4.59±0.09	0.27±0.16	0.06±0.04
	41.2	5.31±0.10	-0.54±0.12	-0.11±0.02
	65.4	5.50±0.11	-1.09±0.13	-0.20±0.02
	87.3	5.46±0.09	-1.48±0.10	-0.28±0.02
	108.6	4.92±0.11	-1.50±0.13	-0.30±0.02
	127.5	4.47±0.11	-1.15±0.13	-0.25±0.03
	145.1	3.88±0.11	-0.62±0.13	-0.16±0.04
	161.3	2.69±0.18	0.10±0.24	0.04±0.09

TABLE II. (*Continued*).

E (MeV)	$\theta_{\text{c.m.}}$ (deg)	$\frac{d\sigma}{d\Omega}(\theta)$ ($\mu\text{b/sr}$)	$\hat{\Sigma}(\theta)$ ($\mu\text{b/sr}$)	$\Sigma(\theta)$
234.5 ± 3.6	16.7	4.69 ± 0.12	-0.20 ± 0.24	-0.04 ± 0.05
	41.4	5.34 ± 0.13	-0.82 ± 0.17	-0.15 ± 0.03
	65.7	5.50 ± 0.16	-0.79 ± 0.19	-0.16 ± 0.03
	87.6	5.64 ± 0.09	-1.73 ± 0.10	-0.31 ± 0.02
	108.9	4.78 ± 0.15	-1.61 ± 0.17	-0.35 ± 0.03
	127.8	4.41 ± 0.14	-1.38 ± 0.17	-0.31 ± 0.04
	145.3	3.68 ± 0.14	-0.68 ± 0.18	-0.18 ± 0.050
	161.4	2.90 ± 0.18	-0.30 ± 0.23	-0.10 ± 0.08
244.4 ± 6.2	16.8	4.67 ± 0.11	-0.17 ± 0.21	-0.04 ± 0.05
	41.5	5.35 ± 0.12	-0.54 ± 0.14	-0.10 ± 0.03
	65.8	5.31 ± 0.15	-1.39 ± 0.17	-0.25 ± 0.03
	87.8	5.68 ± 0.08	-1.80 ± 0.10	-0.31 ± 0.02
	109.1	4.94 ± 0.13	-1.63 ± 0.15	-0.33 ± 0.02
	128.0	4.28 ± 0.13	-1.02 ± 0.15	-0.24 ± 0.04
	145.4	4.14 ± 0.13	-0.71 ± 0.15	-0.17 ± 0.04
	161.5	2.99 ± 0.17	-0.15 ± 0.21	-0.05 ± 0.07
260.5 ± 6.8	16.9	5.05 ± 0.09	-0.22 ± 0.17	-0.04 ± 0.03
	41.8	5.45 ± 0.10	-0.51 ± 0.12	-0.09 ± 0.02
	66.2	5.74 ± 0.12	-1.12 ± 0.13	-0.20 ± 0.02
	88.3	5.72 ± 0.07	-1.81 ± 0.08	-0.32 ± 0.01
	109.6	5.00 ± 0.11	-1.39 ± 0.12	-0.30 ± 0.02
	128.4	4.65 ± 0.10	-1.35 ± 0.11	-0.29 ± 0.03
	145.7	4.11 ± 0.11	-0.30 ± 0.13	-0.07 ± 0.03
	161.7	3.08 ± 0.15	-0.02 ± 0.17	-0.01 ± 0.06
276.3 ± 7.2	17.0	4.94 ± 0.09	0.11 ± 0.15	0.02 ± 0.03
	42.1	5.22 ± 0.09	-0.62 ± 0.10	-0.12 ± 0.02
	66.6	5.31 ± 0.11	-1.05 ± 0.12	-0.21 ± 0.02
	88.7	5.84 ± 0.06	-1.79 ± 0.07	-0.31 ± 0.01
	110.0	4.89 ± 0.10	-1.58 ± 0.11	-0.32 ± 0.02
	128.8	4.45 ± 0.10	-0.91 ± 0.11	-0.20 ± 0.02
	146.0	3.92 ± 0.11	-0.35 ± 0.12	-0.09 ± 0.03
	161.9	3.09 ± 0.13	0.07 ± 0.15	0.02 ± 0.05
290.9 ± 4.6	17.1	4.71 ± 0.10	-0.21 ± 0.17	-0.04 ± 0.03
	42.3	5.00 ± 0.10	-0.40 ± 0.12	-0.08 ± 0.02
	67.0	5.13 ± 0.13	-1.29 ± 0.14	-0.24 ± 0.03
	89.1	5.45 ± 0.07	-1.54 ± 0.07	-0.28 ± 0.01
	110.5	4.79 ± 0.12	-1.43 ± 0.13	-0.30 ± 0.02
	129.2	4.08 ± 0.12	-0.75 ± 0.13	-0.18 ± 0.03
	146.3	3.97 ± 0.12	-0.40 ± 0.14	-0.10 ± 0.03
	162.0	3.11 ± 0.16	-0.09 ± 0.18	-0.03 ± 0.06
300.4 ± 5.0	17.2	4.71 ± 0.11	0.16 ± 0.19	0.03 ± 0.04
	42.5	4.53 ± 0.12	-0.39 ± 0.14	-0.09 ± 0.03
	67.2	4.93 ± 0.15	-1.08 ± 0.16	-0.22 ± 0.03
	89.4	5.19 ± 0.07	-1.51 ± 0.08	-0.30 ± 0.01
	110.7	4.62 ± 0.14	-1.30 ± 0.15	-0.28 ± 0.02
	129.4	4.36 ± 0.14	-0.78 ± 0.15	-0.18 ± 0.03
	146.5	3.85 ± 0.15	-0.41 ± 0.17	-0.11 ± 0.04
	162.1	3.01 ± 0.19	0.00 ± 0.22	0.00 ± 0.07

TABLE II (*Continued*).

E (MeV)	$\theta_{\text{c.m.}}$ (deg)	$\frac{d\sigma}{d\Omega}(\theta)$ ($\mu\text{b/sr}$)	$\hat{\Sigma}(\theta)$ ($\mu\text{b/sr}$)	$\Sigma(\theta)$
313.8 \pm 7.4	17.3	3.97 \pm 0.20	0.00 \pm 0.37	0.00 \pm 0.09
	42.7	4.61 \pm 0.21	-0.11 \pm 0.25	-0.03 \pm 0.05
	67.5	3.83 \pm 0.30	-0.98 \pm 0.33	-0.32 \pm 0.07
	89.7	4.80 \pm 0.08	-1.54 \pm 0.09	-0.32 \pm 0.02
	111.1	4.37 \pm 0.24	-1.13 \pm 0.27	-0.38 \pm 0.04
	129.7	4.00 \pm 0.25	-0.95 \pm 0.28	-0.23 \pm 0.07
	146.7	2.95 \pm 0.27	-0.30 \pm 0.32	-0.11 \pm 0.11
	162.2	2.63 \pm 0.37	0.10 \pm 0.43	0.08 \pm 0.17

timates for the polarization-independent scale uncertainties ranged from 4–5 % for the various data sets. Since the χ^2 analysis confirms the consistency of the data sets, we conservatively ascribe a uniform scale uncertainty of $\pm 5\%$ to the averaged absolute cross sections, as indicated in the last column of Table I.

The angle integrated total cross sections are found by fitting the averaged angular distributions with Legendre polynomials weighted by the statistical and polarization-dependent systematic uncertainties. These are given in Table IV and plotted in Fig. 21.

H. Comparison with existing data

The averaged data sets agree well with existing monochromatic and quasi-monochromatic data as seen in Figs.

16–20. The agreement with the unpolarized cross sections obtained with monochromatic beams at Bonn and Mainz is overall quite good. Nevertheless, there are still variations near the peak of the Δ where the present work lies closer to the Bonn results. The Frascati quasimonochromatic data, as discussed earlier, lies somewhat above the present work. The comparison with published asymmetry data is also quite good although the older data tends to be more scattered than the present work. The agreement with the recent high precision data from Mainz [35] is excellent. The asymmetry at 75° lab ($\approx 90^\circ$ c.m.) as a function of photon laboratory energy is compared with published data in this energy range in Fig. 20. The agreement is quite good throughout the range spanned by this experiment. There are no existing data with which to compare the polarization-dependent cross sections.

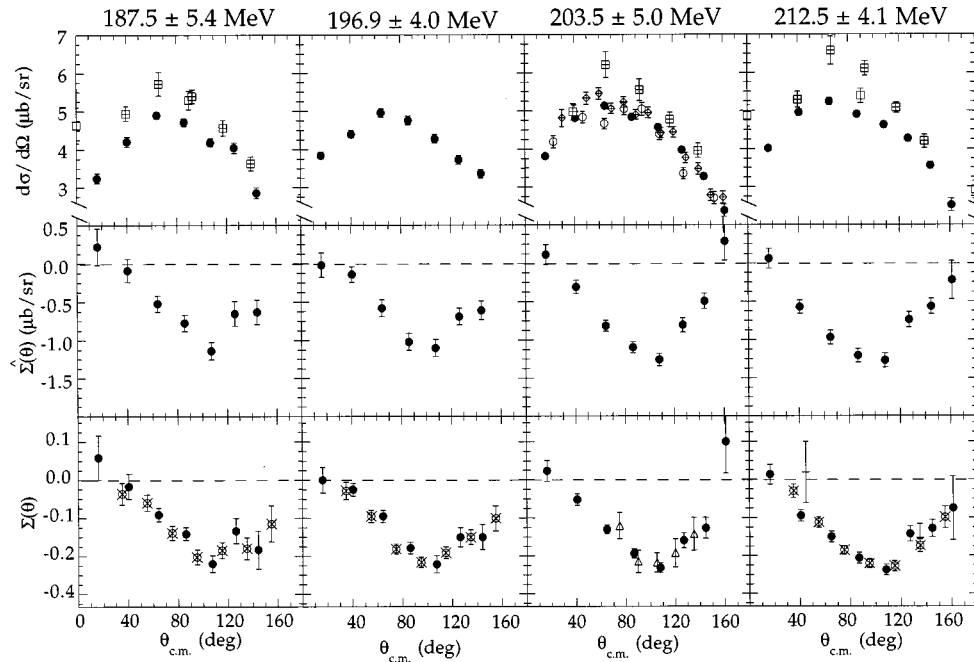


FIG. 16. The unpolarized cross section, the polarization difference, and the beam asymmetry for $E_\gamma = 187.5, 196.9, 203.5,$ and 212.5 MeV. The averaged $L1/L3$ data are shown with filled circles, the open and crossed squares represent the Frascati data [3,15], the open circles are from Bonn [4], the Mainz [5] data are shown with crossed diamonds, data from Khar'kov [33] are shown with open triangles, and asymmetry data from Mainz [35] are shown with crossed circles.

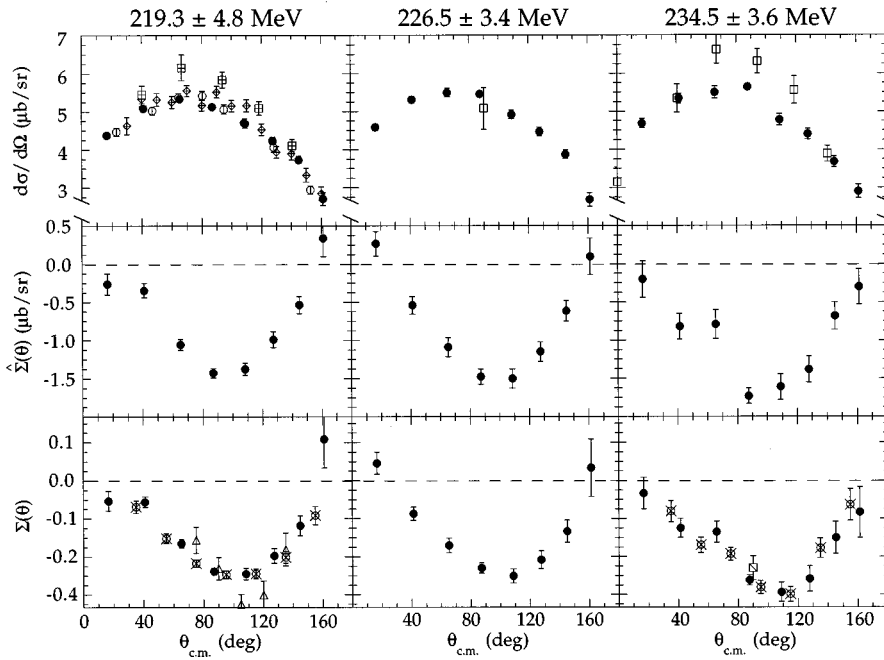


FIG. 17. The same as Fig. 16 for $E_\gamma = 219.3, 226.5,$ and 234.5 MeV. Asymmetry data from Frascati [32] is shown with the slashed square.

As noted in the Introduction, absolute cross sections for the photodisintegration of deuterium have varied by as much as a factor of two in the region around the delta. This situation has improved dramatically since monochromatic and quasimonochromatic photon sources have become available. Figure 21 shows a comparison of the angle integrated total cross sections of the LEGS data set with those of Bonn [4], Mainz [2], Saskatoon [1], and Frascati [3]. The agreement among the data sets obtained with tagged photon sources is now between 1 and 8% depending upon energy.

II. SENSITIVITY TO THE SHORT RANGE PART OF THE NV TENSOR FORCE

A. The Bonn one boson exchange potential

A successful approach to understanding the nucleon-nucleon potential is the field theoretic approach developed by the Bonn group during the decade beginning in the mid 1970s [19]. This model treats the mesons and nucleons as the fundamental fields. The relativistic one boson exchange reduction of the full model in momentum space (OBEPQ)

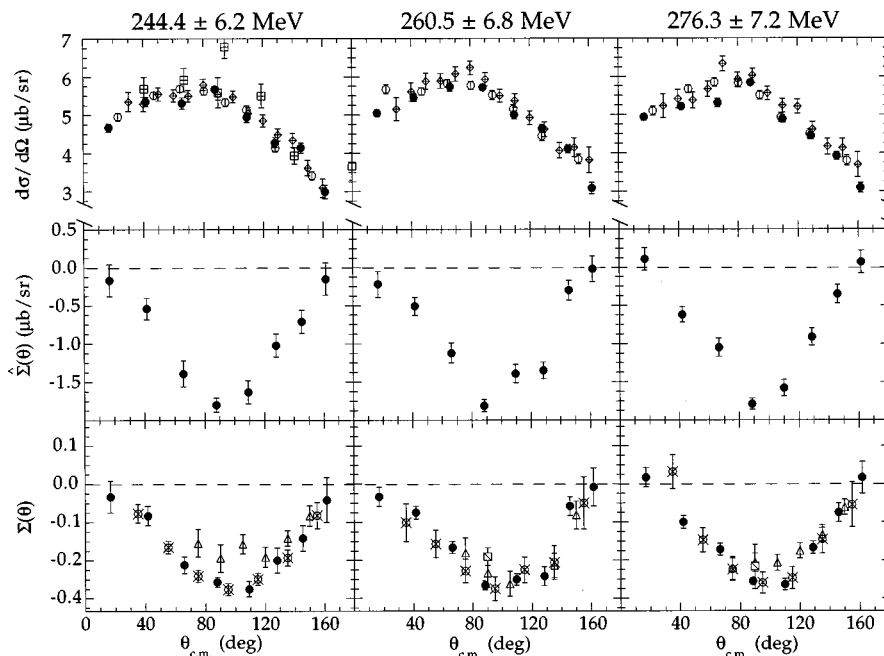


FIG. 18. The same as Fig. 16 for $E_\gamma = 244.4, 260.5,$ and 276.3 MeV.

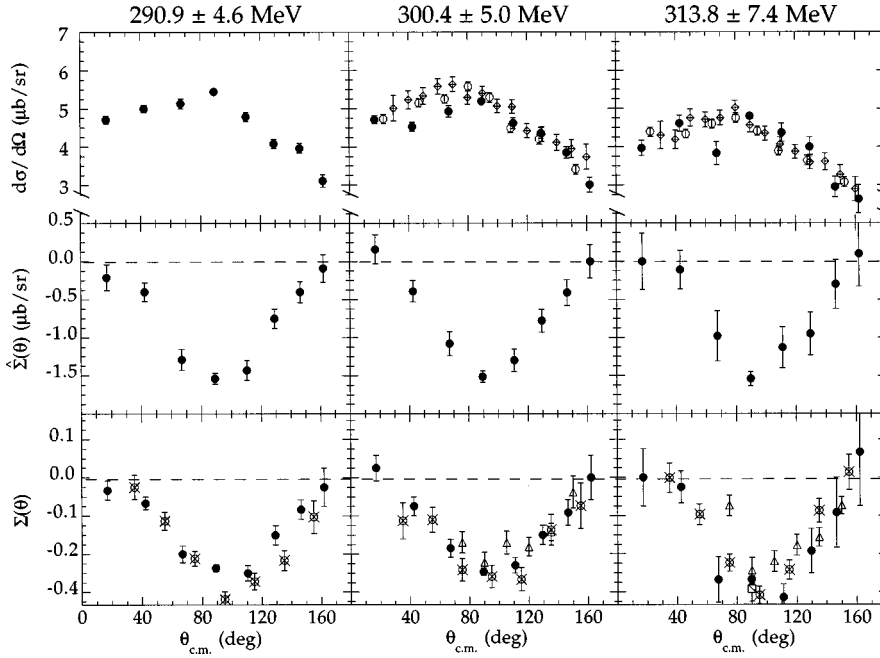


FIG. 19. The same as Fig. 16 for $E_\gamma = 290.9, 300.4,$ and 313.8 MeV.

allows one to describe the long range ($r > 2$ fm) portion of the NN interaction by single pion exchange. At shorter distances ($2 \text{ fm} > r > 1 \text{ fm}$) a fictitious σ meson with a mass of 550 MeV is required to represent the S -wave two pion exchange and the contributions of the $\eta, \rho, \omega, \delta$ mesons become important. In the core region ($r < 1$ fm), in addition to multipion and heavy meson exchanges, the composite nature of the fields begin to become apparent. To account for these complications in the core region and the degrees of freedom not explicitly included in the model, form factors are assigned to the vertices.

Because the long range part of the coupling is given by single pion exchange, the πNN coupling constant, $g_\pi^2/4\pi$, determines the asymptotic D/S state ratio and the quadrupole moment for the deuteron. However, the πNN vertex form factor, parametrized as

$$F(q) = \frac{\Lambda_\pi^2 - m_\pi^2}{\Lambda_\pi^2 + q^2}, \quad (13)$$

introduces a cutoff mass, Λ_π , that determines the effective range of the interaction. Apparently equivalent potentials may be produced with cutoff masses of 1.3, 1.7, and 3.0 GeV. While the choice of Λ_π (after refitting form factors and coupling constants for the heavier mesons) has no effect on the static and low-energy deuteron observables, it has a significant effect on D -state wave function for distances less than 2 fm and hence, on the percentage D state, P_D , in the deuteron wave function. This is summarized in Table V.

Although ρ exchange contributes to the tensor interaction at distances less than 2 fm, π exchange provides the dominant contribution for separations larger than about 0.5 fm. The π and ρ contributions to the potential are of opposite sign and become quite large at short range (> 100 MeV for $r < 0.5$ fm). From Table V we see that as Λ_π increases, Λ_ρ decreases and the ρ coupling increases. This changes the

radial dependence of the interference between these contributions to the tensor force and hence, P_D . Because the strength of the tensor force at short range has a strong effect on calculations of many-body systems, it is important to resolve this ambiguity.

It is useful to clarify the role of the D -state of the deuteron. Amado [20] and Friar [21] have shown that the D -state is not strictly an *observable*. Although any $N-N$ potential model fitted to data will have a definite value for the D -state percentage, another $N-N$ potential can always be constructed that can produce an equivalent fit to the data with a different fraction of D -state, with these values varying generally between 4 and 6% [22]. Nonetheless, within the context of a given potential model, the D -state percentage must be properly adjusted to give a reasonable description of available data. This requirement becomes even more important when an $N-N$ potential is used in a many-body calculation. Various many-body properties, such as the binding energies of the three-body system and the density of nuclear matter, are affected by the D -state of the chosen $N-N$ potential, and the D -state appropriate for the potential can only be fixed by comparing to observables directly sensitive to the strength of the tensor interaction. Two such observables, the polarization-dependent cross section in the photodisintegration of deuteron, $\hat{\Sigma}(\theta)$, and the $n-p$ transition amplitude, ε_1 , are discussed here.

B. $n-p$ scattering

The ambiguities in the isospin zero tensor forces described above may also be examined in $n-p$ scattering. The $\Delta L = 2$ orbital angular momentum transitions, in particular the ${}^3S_1 - {}^3D_1$ transition amplitude, ε_1 , is sensitive to the short range behavior of the tensor force. Such data can, in principle, discriminate among the three OBEPQ potentials described above.

TABLE III. Error weighted average excitation functions obtained from the $L1$ and $L3$ data.

$\theta(\text{deg})_{\text{ab}}$	E_γ (MeV)	$\frac{d\sigma}{d\Omega}$ ($\mu\text{b}/\text{sr}$)	$\hat{\Sigma}$ ($\mu\text{b}/\text{sr}$)	Σ
15	189.0 \pm 4.0	3.24 \pm 0.13	0.22 \pm 0.24	0.07 \pm 0.07
	197.0 \pm 4.0	3.84 \pm 0.09	-0.02 \pm 0.16	0.00 \pm 0.04
	204.0 \pm 4.3	3.82 \pm 0.07	0.12 \pm 0.13	0.03 \pm 0.03
	212.2 \pm 4.2	4.02 \pm 0.07	0.06 \pm 0.13	0.02 \pm 0.03
	219.6 \pm 4.0	4.38 \pm 0.08	-0.26 \pm 0.13	-0.06 \pm 0.03
	226.0 \pm 3.5	4.59 \pm 0.09	0.27 \pm 0.16	0.06 \pm 0.04
	234.0 \pm 3.5	4.69 \pm 0.12	-0.20 \pm 0.24	-0.04 \pm 0.05
	245.0 \pm 7.5	4.67 \pm 0.11	-0.17 \pm 0.21	-0.04 \pm 0.05
	261.0 \pm 7.5	5.05 \pm 0.09	-0.22 \pm 0.17	-0.04 \pm 0.03
	277.0 \pm 8.5	4.94 \pm 0.09	0.11 \pm 0.15	0.02 \pm 0.03
	290.0 \pm 4.5	4.71 \pm 0.10	-0.21 \pm 0.17	-0.04 \pm 0.03
	299.0 \pm 5.0	4.71 \pm 0.11	0.16 \pm 0.19	0.03 \pm 0.04
	315.0 \pm 11	3.97 \pm 0.20	0.00 \pm 0.37	0.00 \pm 0.09
	35	189.0 \pm 4.0	4.20 \pm 0.13	-0.09 \pm 0.15
197.0 \pm 4.0		4.40 \pm 0.10	-0.14 \pm 0.10	-0.030 \pm 0.02
204.4 \pm 4.2		4.81 \pm 0.08	-0.31 \pm 0.09	-0.062 \pm 0.02
212.6 \pm 4.1		4.96 \pm 0.08	-0.57 \pm 0.09	-0.114 \pm 0.02
219.7 \pm 4.0		5.08 \pm 0.08	-0.34 \pm 0.09	-0.067 \pm 0.02
226.0 \pm 3.5		5.31 \pm 0.10	-0.54 \pm 0.12	-0.105 \pm 0.02
234.0 \pm 3.5		5.34 \pm 0.13	-0.82 \pm 0.17	-0.150 \pm 0.03
245.0 \pm 7.5		5.35 \pm 0.12	-0.54 \pm 0.14	-0.100 \pm 0.03
261.0 \pm 7.5		5.45 \pm 0.10	-0.51 \pm 0.12	-0.090 \pm 0.02
277.0 \pm 8.5		5.22 \pm 0.09	-0.62 \pm 0.10	-0.120 \pm 0.02
290.0 \pm 4.5		5.00 \pm 0.10	-0.40 \pm 0.12	-0.080 \pm 0.02
299.0 \pm 5.0		4.53 \pm 0.12	-0.39 \pm 0.14	-0.090 \pm 0.03
315.0 \pm 11		4.61 \pm 0.21	-0.11 \pm 0.25	-0.030 \pm 0.05
55		113.0 \pm 16	5.97 \pm 0.13	0.10 \pm 0.30
	137.0 \pm 8.0	5.51 \pm 0.15	0.06 \pm 0.25	0.01 \pm 0.05
	152.6 \pm 7.7	5.64 \pm 0.14	0.08 \pm 0.20	0.01 \pm 0.04
	160.0 \pm 8.0			0.13 \pm 0.09
	170.1 \pm 8.0	5.61 \pm 0.13	-0.33 \pm 0.17	-0.07 \pm 0.03
	187.0 \pm 5.9	4.90 \pm 0.09	-0.52 \pm 0.11	-0.11 \pm 0.02
	196.9 \pm 4.0	4.96 \pm 0.11	-0.58 \pm 0.11	-0.11 \pm 0.02
	202.9 \pm 5.8	5.14 \pm 0.07	-0.82 \pm 0.07	-0.16 \pm 0.01
	212.6 \pm 4.1	5.24 \pm 0.09	-0.97 \pm 0.09	-0.18 \pm 0.02
	218.6 \pm 5.7	5.33 \pm 0.07	-1.06 \pm 0.07	-0.20 \pm 0.01
	226.0 \pm 3.6	5.50 \pm 0.11	-1.09 \pm 0.13	-0.20 \pm 0.02
	234.6 \pm 3.6	5.50 \pm 0.16	-0.79 \pm 0.19	-0.16 \pm 0.03
	244.8 \pm 6.8	5.31 \pm 0.15	-1.39 \pm 0.17	-0.25 \pm 0.03
	252.0 \pm 4.0			-0.21 \pm 0.06
	260.9 \pm 7.2	5.74 \pm 0.12	-1.12 \pm 0.13	-0.20 \pm 0.02
	268.0 \pm 4.0			-0.24 \pm 0.06
	276.9 \pm 7.9	5.31 \pm 0.11	-1.05 \pm 0.12	-0.21 \pm 0.02
	284.0 \pm 4.0			-0.24 \pm 0.05
	290.4 \pm 4.4	5.13 \pm 0.13	-1.29 \pm 0.14	-0.24 \pm 0.03
	299.2 \pm 4.9	4.93 \pm 0.15	-1.08 \pm 0.16	-0.22 \pm 0.03
314.0 \pm 10	3.83 \pm 0.30	-0.98 \pm 0.33	-0.32 \pm 0.07	

TABLE III (*Continued*).

$\theta(\text{deg})_{\text{ab}}$	E_γ (MeV)	$\frac{d\sigma}{d\Omega}$ ($\mu\text{b/sr}$)	$\hat{\Sigma}$ ($\mu\text{b/sr}$)	Σ
75	113.0±16.0	4.71±0.12	0.42±0.29	0.09±0.06
	137.0±8.0	4.74±0.15	0.25±0.26	0.05±0.05
	152.2±7.4	4.24±0.14	-0.23±0.19	-0.04±0.05
	160.0±8.0			-0.08±0.07
	171.4±8.0	4.62±0.13	-0.68±0.17	-0.17±0.03
	187.1±5.8	4.71±0.10	-0.78±0.11	-0.17±0.02
	196.9±4.0	4.76±0.11	-1.02±0.11	-0.21±0.02
	203.4±5.1	4.84±0.07	-1.10±0.07	-0.23±0.01
	212.5±4.1	4.90±0.08	-1.21±0.09	-0.25±0.02
	219.6±4.8	5.12±0.05	-1.43±0.06	-0.29±0.01
	227.4±3.1	5.46±0.09	-1.48±0.10	-0.28±0.02
	234.9±3.7	5.64±0.09	-1.73±0.10	-0.31±0.02
	243.7±4.9	5.68±0.08	-1.80±0.09	-0.31±0.02
	250.4±3.8	5.82±0.10	-1.74±0.12	-0.29±0.02
	259.6±5.6	5.72±0.07	-1.81±0.08	-0.32±0.01
	266.2±4.1	5.80±0.10	-1.95±0.11	-0.34±0.01
	275.1±5.6	5.84±0.06	-1.79±0.07	-0.31±0.01
	283.1±4.5	5.73±0.09	-1.68±0.10	-0.30±0.01
	291.7±4.7	5.44±0.07	-1.54±0.07	-0.28±0.01
	301.7±5.1	5.19±0.07	-1.51±0.08	-0.30±0.01
313.6±6.3	4.80±0.08	-1.54±0.09	-0.32±0.02	
325.0±6.1	4.31±0.14	-1.38±0.15	-0.32±0.03	
95	113.0±16	4.36±0.13	-0.61±0.31	-0.14±0.07
	137.0±8.0	4.52±0.17	-0.25±0.28	-0.06±0.06
	152.3±7.5	4.22±0.15	-0.81±0.22	-0.17±0.05
	160.0±8.0			-0.23±0.07
	171.2±8.0	4.25±0.14	-0.73±0.18	-0.21±0.03
	187.1±5.7	4.18±0.10	-1.14±0.11	-0.26±0.03
	196.8±4.0	4.28±0.11	-1.10±0.11	-0.27±0.03
	203.5±5.1	4.57±0.07	-1.26±0.08	-0.28±0.02
	212.5±4.1	4.63±0.09	-1.27±0.09	-0.29±0.02
	218.7±5.4	4.70±0.08	-1.37±0.08	-0.29±0.02
	226.1±3.6	4.92±0.11	-1.50±0.13	-0.30±0.02
	234.7±3.7	4.78±0.15	-1.61±0.17	-0.35±0.03
	244.7±6.3	4.94±0.13	-1.63±0.15	-0.33±0.02
	252.0±4.0			-0.29±0.04
	260.8±6.8	5.00±0.11	-1.39±0.12	-0.30±0.02
	268.0±4.0			-0.33±0.04
	276.8±7.6	4.89±0.10	-1.58±0.11	-0.32±0.02
	284.0±4.0			-0.33±0.04
	290.7±4.3	4.79±0.12	-1.43±0.13	-0.30±0.02
	299.4±4.7	4.62±0.14	-1.30±0.15	-0.28±0.02
313.5±9.5	4.37±0.24	-1.13±0.27	-0.38±0.04	

TABLE III (Continued).

$\theta(\text{deg})_{\text{ab}}$	E_γ (MeV)	$\frac{d\sigma}{d\Omega}$ ($\mu\text{b}/\text{sr}$)	$\hat{\Sigma}$ ($\mu\text{b}/\text{sr}$)	Σ
115	189.0 \pm 4.0	4.04 \pm 0.14	-0.65 \pm 0.16	-0.16 \pm 0.04
	197.0 \pm 4.0	3.72 \pm 0.11	-0.69 \pm 0.11	-0.18 \pm 0.03
	203.9 \pm 4.3	3.98 \pm 0.08	-0.81 \pm 0.09	-0.19 \pm 0.02
	212.3 \pm 4.2	4.27 \pm 0.09	-0.74 \pm 0.10	-0.17 \pm 0.02
	219.6 \pm 4.0	4.24 \pm 0.10	-0.99 \pm 0.11	-0.24 \pm 0.02
	226.0 \pm 3.5	4.47 \pm 0.11	-1.15 \pm 0.13	-0.25 \pm 0.03
	234.0 \pm 3.5	4.41 \pm 0.14	-1.38 \pm 0.17	-0.31 \pm 0.04
	245.0 \pm 7.5	4.28 \pm 0.13	-1.02 \pm 0.15	-0.24 \pm 0.04
	261.0 \pm 7.5	4.65 \pm 0.10	-1.35 \pm 0.11	-0.29 \pm 0.03
	277.0 \pm 8.5	4.45 \pm 0.10	-0.91 \pm 0.11	-0.20 \pm 0.02
	290.0 \pm 4.5	4.08 \pm 0.12	-0.75 \pm 0.13	-0.18 \pm 0.03
	299.0 \pm 5.0	4.36 \pm 0.14	-0.78 \pm 0.15	-0.18 \pm 0.03
	315.0 \pm 11	4.00 \pm 0.25	-0.95 \pm 0.28	-0.23 \pm 0.07
135	189.0 \pm 4.0	2.85 \pm 0.14	-0.63 \pm 0.16	-0.22 \pm 0.06
	197.0 \pm 4.0	3.36 \pm 0.11	-0.61 \pm 0.12	-0.18 \pm 0.04
	204.0 \pm 4.3	3.28 \pm 0.08	-0.49 \pm 0.10	-0.15 \pm 0.03
	212.6 \pm 4.1	3.57 \pm 0.09	-0.56 \pm 0.10	-0.15 \pm 0.03
	219.6 \pm 4.0	3.73 \pm 0.10	-0.54 \pm 0.11	-0.14 \pm 0.03
	226.0 \pm 3.5	3.88 \pm 0.11	-0.62 \pm 0.13	-0.16 \pm 0.04
	234.0 \pm 3.5	3.68 \pm 0.14	-0.68 \pm 0.18	-0.18 \pm 0.05
	245.0 \pm 7.5	4.14 \pm 0.13	-0.71 \pm 0.15	-0.17 \pm 0.04
	261.0 \pm 7.5	4.11 \pm 0.11	-0.30 \pm 0.13	-0.07 \pm 0.03
	277.0 \pm 8.5	3.92 \pm 0.11	-0.35 \pm 0.12	-0.09 \pm 0.03
	290.0 \pm 4.5	3.97 \pm 0.12	-0.40 \pm 0.14	-0.10 \pm 0.03
	299.0 \pm 5.0	3.85 \pm 0.15	-0.41 \pm 0.17	-0.11 \pm 0.04
	315.0 \pm 11	2.95 \pm 0.27	-0.30 \pm 0.32	-0.11 \pm 0.11
155	202.0 \pm 5.0	2.38 \pm 0.16	0.29 \pm 0.25	0.12 \pm 0.10
	211.0 \pm 4.5	2.52 \pm 0.17	-0.22 \pm 0.25	-0.09 \pm 0.10
	219.0 \pm 4.0	2.71 \pm 0.17	0.34 \pm 0.24	0.13 \pm 0.09
	227.0 \pm 3.5	2.69 \pm 0.18	0.10 \pm 0.24	0.04 \pm 0.09
	234.0 \pm 3.5	2.90 \pm 0.18	-0.30 \pm 0.23	-0.10 \pm 0.08
	245.0 \pm 7.5	2.99 \pm 0.17	-0.15 \pm 0.21	-0.05 \pm 0.07
	261.0 \pm 7.5	3.08 \pm 0.15	-0.02 \pm 0.17	-0.01 \pm 0.06
	277.0 \pm 8.5	3.09 \pm 0.13	0.07 \pm 0.15	0.02 \pm 0.05
	290.0 \pm 4.5	3.11 \pm 0.16	-0.09 \pm 0.18	-0.03 \pm 0.06
	299.0 \pm 5.0	3.01 \pm 0.19	0.00 \pm 0.22	0.00 \pm 0.07
315.0 \pm 11	2.63 \pm 0.37	0.10 \pm 0.43	0.08 \pm 0.17	

The ability to make such a discrimination in the face of the statistical and systematic uncertainties has been examined in detail by Chulick *et al.* [6]. By far the most extensive n - p scattering data set exists at a laboratory energy of 325 MeV (2030 MeV in the n - p c.m.). This and the ambiguities at lower energies have emphasized the importance of the 325 MeV data. Chulick *et al.* find that a proper handling of the uncertainties and correlations leads to a large uncertainty on ε_1 . The poor determination of this crucial parameter places very little constraint on the strength of the tensor interaction. The results of phase shift analyses are compared with calculations using the Bonn potentials A , B , and C as well as the full Bonn [25] and the Paris [26] potentials in Fig. 23. While potentials B and C seem to reproduce the trend of the data

better than A , the uncertainty of the most precisely determined point, indicates that this comparison places little or no constraint on the tensor force.

C. Deuteron photodisintegration

As suggested by the energy scale across the top of Fig. 22, photodisintegration data in region near 200 MeV is also a potentially fertile place to seek information about the tensor interaction. Schmitt and Arenhövel [25] have calculated this reaction using the Bonn OBEPQ potentials. These calculations include static π and ρ exchange currents, isobar currents in the impulse approximation, the relativistic spin-orbit current, and the lowest order relativistic corrections to the

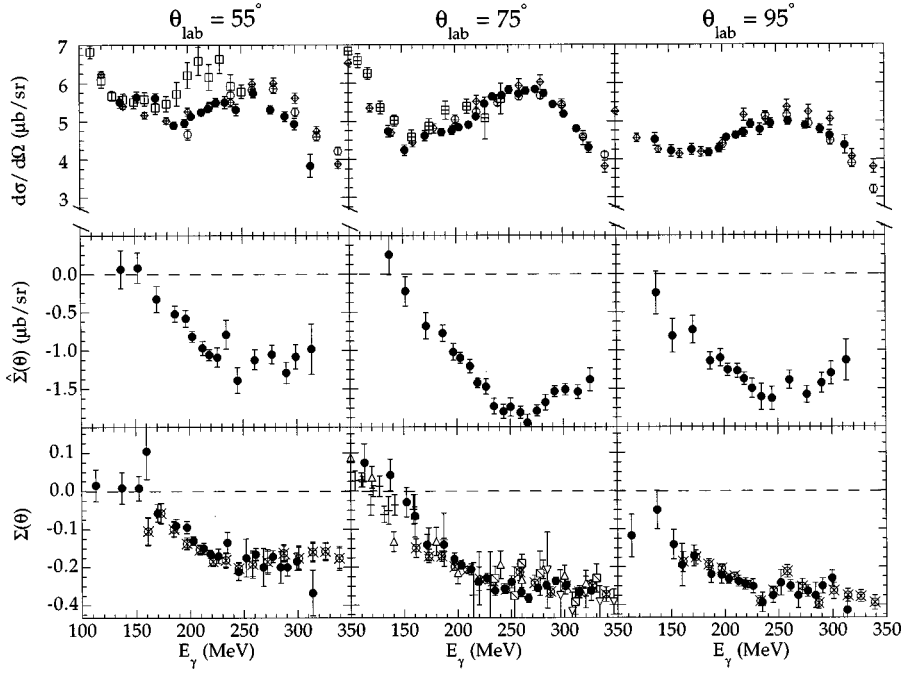


FIG. 20. Excitation functions for the three angles at which NSS data were taken below the tagging threshold. The crosses represent data from Stanford [31] and the inverted triangles indicate data from Yerevan [34] and the other symbols have the same meaning as in Figs. 16 and 17. The Bonn cross section data shown at $\theta_{\text{lab}} = 75^\circ$ are the average of the $\theta_{\text{lab}} = 68.0^\circ$ and 81.6° data and the Mainz 55° cross sections are the average of the $\theta_{\text{c.m.}} = 60^\circ$ and 70° data. The Mainz asymmetries shown at 55° are the average of the $\theta_{\text{c.m.}} = 55^\circ$ and 75° data, the 75° data is the average of the $\theta_{\text{c.m.}} = 75^\circ$ and 95° data, and the 95° data is the average of the $\theta_{\text{c.m.}} = 95^\circ$ and 115° data.

one-body currents. The comparison of these calculations with the LEGS data is shown in Fig. 23.

The calculations using parametrization *B* (long-dashed curves) give reasonable agreement with $\Sigma(\theta)$. However, the comparison with $d\sigma(\theta)/d\Omega$ and $\hat{\Sigma}(\theta)$ separately show this agreement to be fortuitous. The absolute cross sections are significantly underestimated. Furthermore, we see that the various calculations of $d\sigma(\theta)/d\Omega$ are indistinguishable and only $\hat{\Sigma}(\theta)$ displays any sensitivity to the tensor interaction. Thus it is to $\hat{\Sigma}(\theta)$ that comparisons should really be made, not the mixture the asymmetry represents. The polarization-dependent cross section, $\hat{\Sigma}(\theta)$, provides the necessary sensitivity to the tensor interaction and the uncertainties in the photodisintegration data are small enough to permit a meaningful discrimination among the models. The agreement with $\hat{\Sigma}(\theta)$ appears to be good except near 90° . However, this

agreement can be misleading. Since the azimuthal scattering angle is undefined at 0° and 180° and this observable must vanish at the extreme angles, appreciable differences are possible only near 90° . Hence, it is the disagreement around 90° not the agreement at the extreme angles that is important.

Although parametrization *C* gives a fairly reasonable result for the polarization dependent cross section, until better agreement is obtained for both the polarization-independent

TABLE IV. Angle integrated cross sections from Legendre polynomial fits to the averaged angular distribution in Table II.

E_γ (MeV)	σ (μb)
190.8	52.4 ± 0.6
201.2	55.3 ± 0.4
210.8	56.8 ± 0.4
220.6	59.8 ± 0.4
226.7	60.3 ± 0.7
234.1	61.4 ± 0.7
245.3	62.4 ± 0.6
260.5	64.3 ± 0.5
276.6	62.4 ± 0.5
289.7	59.6 ± 0.6
299.3	57.6 ± 0.7
315.1	53.2 ± 1.2

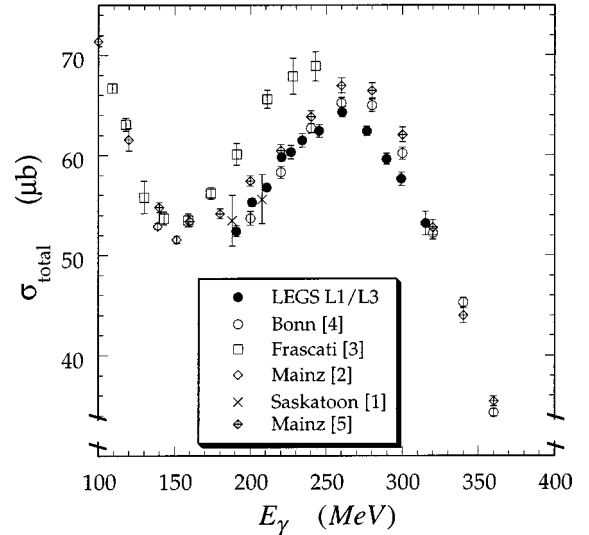


FIG. 21. The angle integrated cross sections for the photodisintegration of deuterium for the averaged data from LEGS experiments *L1* and *L3* compared to previous data. The LEGS data are represented by the filled circles. The other symbols have the same meaning as in Fig. 1. The error bars on the LEGS data reflect the statistical and polarization-dependent systematic uncertainties and are generally smaller than the plotting symbols. Note the suppressed zero on the vertical scale.

TABLE V. The effect of varying the cutoff mass in the πNN vertex factor [19]. The cutoff mass and the coupling strength of the ρNN vertex and the percentage D state, P_D , are also listed for comparison. The πNN coupling strength, the quadrupole moment, and the asymptotic D/S ratio are constrained by data.

Potential	Λ_π (GeV)	$g_\pi^2/4\pi$	Λ_ρ (GeV)	$g_\rho^2/4\pi$	P_D (%)	Q (fm ²)	D/S
A	1.3	14.7	1.95	0.86	4.4	0.274	0.0263
B	1.7	14.4	1.85	0.9	5.0	0.278	0.0264
C	3.0	14.2	1.7	1.0	5.6	0.281	0.0266

and dependent cross sections, it is premature to adjust the cutoff mass to fit the data. The disagreement with the shape and magnitude of the polarization-independent cross section is most troubling. The predicted shape of the angular distribution is strongly affected by the relativistic spin-orbit current [26]. This current produces strong effects at 0° and 180° , but has little effect near 90° , thus cannot be responsible for the discrepancies in $d\sigma(\theta)/d\Omega$.

Calculations using the Paris potential reproduce $\Sigma(\theta)$ and $\tilde{\Sigma}(\theta)$ as well as those using the Bonn potential and, in addition, provide a significantly improved description of the unpolarized cross sections. In this potential, the short range ($r \leq 0.8$ fm) potential is not described by the inclusion of the heavier mesons but rather by a constant soft core with different empirically determined strengths for the central, spin-spin, tensor, spin-orbit, and quadratic spin-orbit components for each isospin [27]. That this purely phenomenological po-

tential does so well indicates that the Bonn potential omits some essential physics. In the next section, we consider the effect of adding explicit Δ degrees of freedom to the calculation.

III. $NN/N\Delta$ COUPLED-CHANNEL CALCULATIONS

Because of the strong $M1$ photon coupling to the delta and the strong decay of the delta into the πN channels, it is important to go beyond the impulse approximation to investigate the effect of coupled channels on the agreement with the absolute cross sections. Leidemann and Arenhövel [7] noted that both the cross section and asymmetry are sensitive to the $N\Delta$ interaction. Because both observables were measured simultaneously at LEGS, we are in a unique position to investigate the sensitivities to the $N\Delta$ interaction in the delta region.

Wilhelm and Arenhövel [28] have investigated the effects of Δ dynamics in a momentum space coupled-channels model which includes static π -exchange currents. In this model the $\gamma N\Delta$ coupling is parametrized in two different ways. The first method assumes a decomposition of the elementary M_{1+} (isospin 3/2) γN multipole into Born and resonant terms. Parametrizing the resonant part as a Breit-Wigner shape, the strength is fit to the $N(\gamma, \pi)$ data. By using a complex, energy dependent coupling, unitarity is preserved and the effects of π rescattering can be effectively included. A comparison of this fit to the data [10,28] shows a significant underestimate of the data. This underestimate is most readily seen in a comparison with the angle integrated cross sections (the dotted curve in Fig. 24).

Tanabe and Ohta [29] and Lee [30] have constructed coupled channels models using similar methods to fix the elementary amplitudes in terms of Born and resonant parts. Using a real $\gamma N\Delta$ coupling and explicitly including rescattering to leading order, results very similar to that shown with the dotted line in Fig. 24 are obtained.

In the second method of Ref. [28], the Born terms are dropped from the γN amplitudes. This purely resonant version of the elementary $\gamma N\Delta$ coupling is then refit to the $N(\gamma, \pi)$ data. This approach leads to a double counting in the π -exchange currents to the extent to which they are already included in the $\gamma N\Delta$ coupling. To estimate the size of the double counting error, the π -exchange current contribution to the M_{1+} can be switched off completely. This gives an upper limit to the theoretical uncertainty of a few percent. This method gives a much better representation of the angle integrated cross sections (bounded by solid line in Fig. 24). The significantly improved agreement observed when drop-

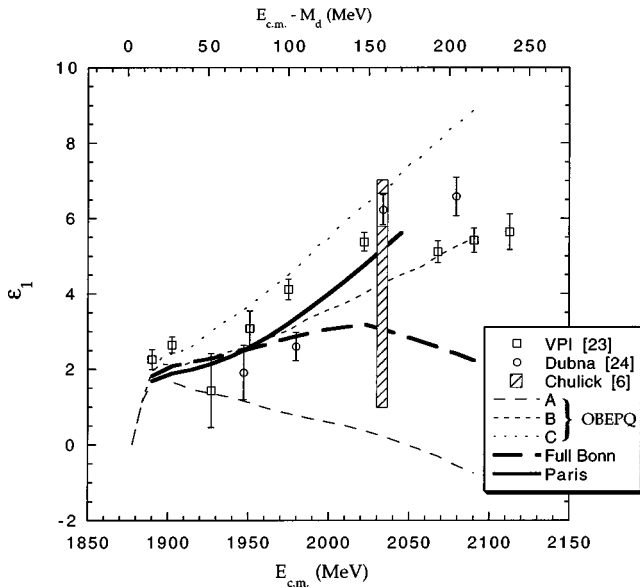


FIG. 22. The 3S_1 - 3D_1 mixing parameter, ε_1 , as a function of laboratory energy in the n - p system. The scale across the top, the total center of mass energy of the system minus the rest mass of the deuteron, is the corresponding center of mass photon energy for the photodisintegration reaction. The experimental determinations are from VPI [23] (squares) and Dubna [24] (circles). The dot-dashed, short dashed, and long dashed curves represent the OBEPQ potentials A, B, C, respectively [25], and the solid curve uses the Paris potential [26]. The error bar on the point derived from the 325 MeV n - p scattering data ($E_{c.m.} = 2034$ MeV) represents both statistical (inner caps) and systematic (outer caps) uncertainties.

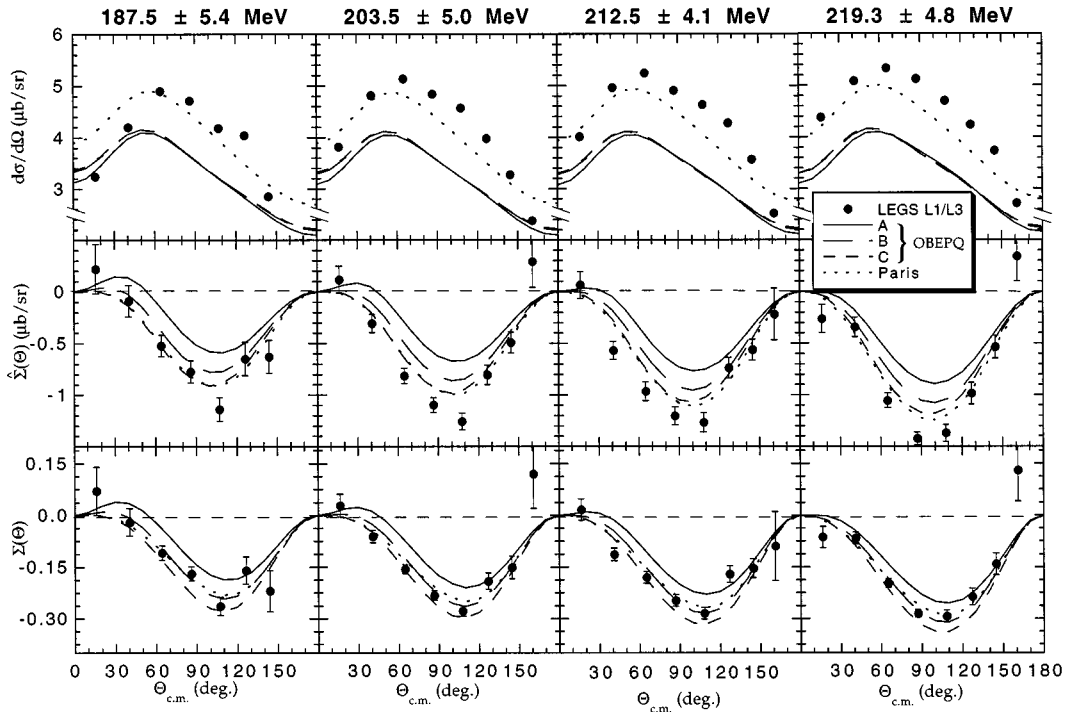


FIG. 23. The $L1/L3$ averaged polarization-independent and polarization-dependent cross sections and the beam asymmetry compared to the calculations using the Bonn OBEPQ potentials A , B , and C and the Paris potential as described in the text. The OBEPQ calculations using potentials A , B , and C are shown with solid, long-dashed, and short-dashed lines, respectively. The Paris potential calculations are indicated with dotted lines.

ping the explicit Born terms and refitting the $\gamma N\Delta$ coupling points to a significant deficiency in the model. Wilhelm and Arenhövel speculate that this may be a signal for nonlocal effects and an incomplete treatment of meson exchange [28].

Although the total cross section is much improved by the resonant only parametrization, it is clear that this is still insufficient. While the calculated total cross sections are above the data near the peak of the delta, the prediction at 90° , shown in Fig. 25, are consistently low for both the polarization-independent and polarization-dependent cross sections near the peak of the delta. Thus, once again the apparent agreement in the beam asymmetry is seen to be misleading when high quality, simultaneously measured absolute cross sections are available. The previously published beam asymmetry data shown were obtained using coherent bremsstrahlung in diamond and typically have large uncertainties.

This agreement with the integrated cross sections and the discrepancy with the 90° excitation function is the result of a depression in the angular distribution near 90° that increases with energy (see Fig. 26 for $E_\gamma = 300$ MeV). As noted in Ref. [10], a similar depression near 90° is a common feature of most calculations near 300 MeV, even when a coupled channels treatment is not used [36,37]. In the work of Tanabe and Ohta [29], this dip was considerably more pronounced than that shown here, being accentuated by an improper treatment of NN phase shifts for $L \geq 1$. While this problem was corrected in the calculations of Lee [30], a depression, reduced in magnitude, remains. Similarly, the work of Peña *et al.* [8] exhibits a much smaller dip, similar to that in Ref. [7]. How-

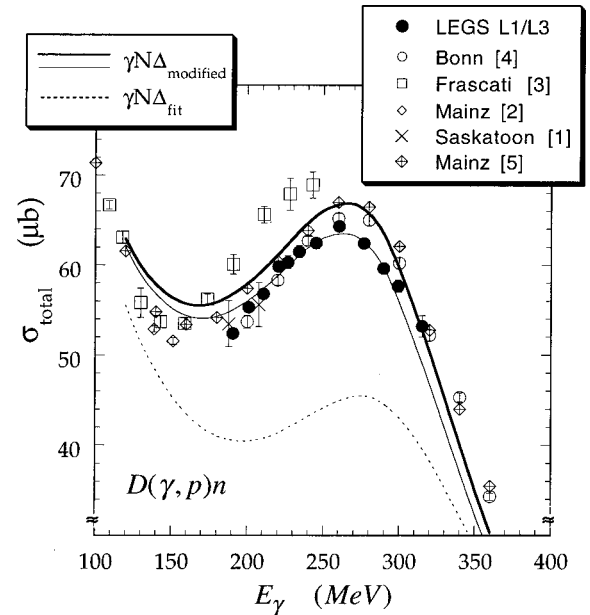


FIG. 24. Comparison of the angle integrated cross sections with the coupled channel calculations. The LEGS data are shown as filled circles and previous data are shown as open symbols and crosses. The dotted curve represents the first method of parametrizing the elementary M_{1+} (isospin 3/2) $\gamma N\Delta$ coupling (Born+Breit-Wigner). The second method (resonant M_{1+} only) is indicated by the solid curves. The region bounded by the solid lines represents the uncertainty in the π -exchange current contribution due to double counting as described in the text.

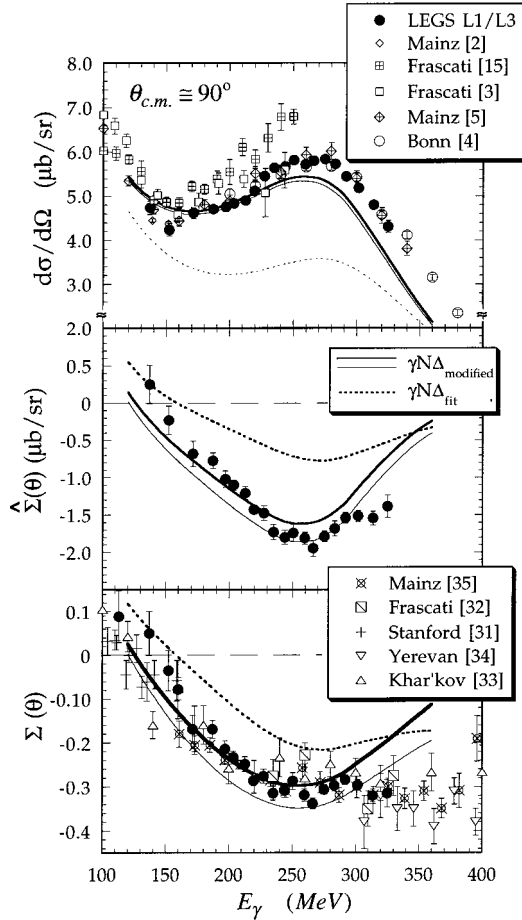


FIG. 25. The excitation functions for $\theta_{c.m.} \approx 90^\circ$. The top and center panels show the polarization-independent and polarization-dependent cross sections, respectively, and the bottom panel shows the beam asymmetry. The curves have the same meaning as in Fig. 24. The LEGS data is shown with the filled circles. Polarization-independent cross sections from Refs. [2,4,15,3] are shown with open symbols in the top panel. The open symbols in the bottom panel represent beam asymmetries from Refs. [31–34].

ever, in both of these works the relativistic spin-orbit currents were omitted, distorting the angular shape. Thus, this depression near 90° is seen to be a common feature of photodisintegration calculations the origin of which is not yet fully understood.

We have previously observed [10] that further insight into the origins of this dip may be found by examining the cross sections obtained with the beam polarization parallel, σ_{\parallel} , and perpendicular, σ_{\perp} . In Fig. 26, the shape of σ_{\parallel} is seen to be well reproduced by both methods of determining the $\gamma N\Delta$ coupling. The dip is seen only in the predictions for σ_{\perp} . One might expect interference with the Born terms, which contain high angular momentum components, to be a possible source of the dip. This cannot be the case since both methods of fixing the $\gamma N\Delta$ coupling produce similar depressions and the resonance-only method does not explicitly include these terms.

Since the elementary multipoles are mixed in the transformation from the γN to the γD systems, deficiencies in the

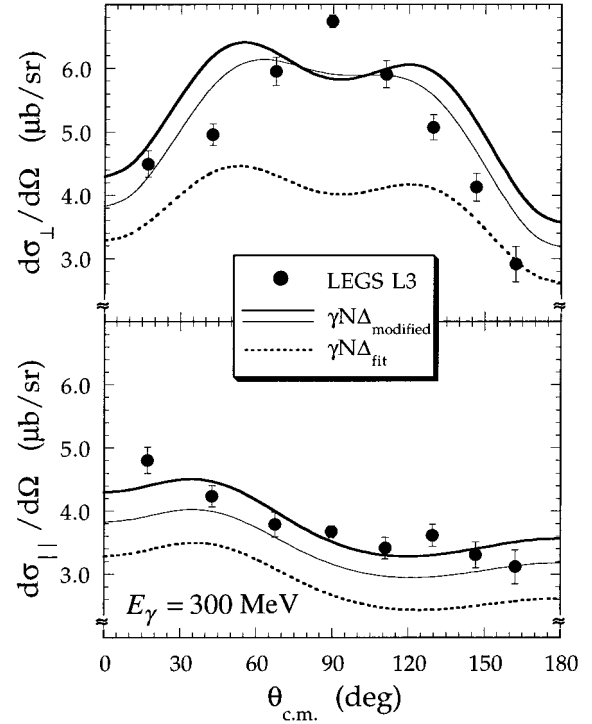


FIG. 26. Angular distributions observed with linear photon polarization parallel and perpendicular to the reaction plane at $E_{\gamma} = 300$ MeV. The curves have the same meaning as in Fig. 25.

calculations can be difficult to isolate. One way to make a more detailed comparison of data and calculation is by a multipole analysis of the data. Whisnant *et al.* [38] have performed such an analysis including electric and magnetic dipole and quadrupole photons in the initial state and all possible relative p - n angular momenta in the final state. The difference between the fit to the data and a fit to the coupled-channels calculation, appears only in magnetic multipoles. The presence or absence of the “dip” may arise from the combination of many different magnetic multipoles but is seen most strongly in the $M2(^3P_2) \cdot M2(^3F_3)$ interference term and its interplay with the dominant $M1(^1D_2)$ term. This dominance of the magnetic multipoles in σ_{\perp} and a corresponding dominance of the electric multipoles in σ_{\parallel} leads to the observed angular shapes. The sensitivity of the “dip” to magnetic multipoles reinforces the suspicion that the problem may lie with the treatment of the MEC’s since the technique used in Ref. [28] relies on Siegert’s theorem to evaluate them. Without explicit knowledge of the nuclear current, this technique can only specify the electric contributions.

In both methods of fixing the $\gamma N\Delta$ coupling, static NN potentials were assumed with meson retardation effects included only in the $N\Delta$ and $NN \rightarrow N\Delta$ transition potentials. The recent coupled-channels calculations of Schwamb *et al.* [39] have added retarded MEC potentials. To maintain unitarity above the 2π threshold, the possibility of both nucleons being on-shell must be admitted. This is done by considering the formation of an intermediate NN state with the quantum numbers of the deuteron and a spectator π . The net effect is to correct the underprediction of the angle integrated

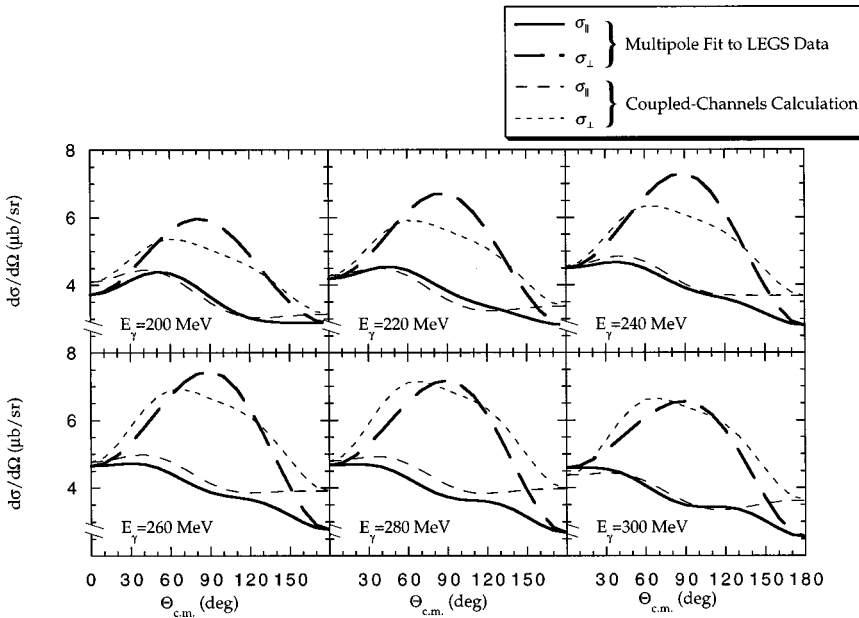


FIG. 27. Comparison of the multipole analysis of the LEGS data by Whisnant *et al.* [38] with the coupled-channels calculations of Schwamb *et al.* [39]. The heavy solid and long-dashed lines represent the fit to the data. The width of the line is comparable to the statistical and polarization dependent uncertainties in the data. The light dashed lines represent the calculation. The lower pair of curves in each panel represents σ_{\parallel} and the upper pair represents σ_{\perp} .

cross sections seen in Fig. 24, leading to a significant improvement in the shape of the angular distribution.

The multipole analysis of the $L1/L3$ data provides a convenient way to make a systematic comparison of data with these calculations. The comparison of σ_{\parallel} and σ_{\perp} calculated by Schwamb [39] with the multipole fit to the data [38] is shown in Fig. 27. For energies above and below the peak of the Δ (260–280 MeV) the fit and calculated σ_{\parallel} agree reasonably well except at large angles where a divergence that increases with energy is observed. However, the calculated σ_{\perp} peaks at a more forward angle than the data at all energies. At the higher energies, the “dip” previously seen in the σ_{\perp} calculations is now reduced to a flattening of the cross section. Near the peak of the Δ , both σ_{\perp} and σ_{\parallel} calculated cross sections show significant differences from the data.

Schwamb *et al.* note that the retarded hadronic currents lower the angle integrated cross section, while the retarded MEC’s and the intermediate on-shell $NN-\pi$ state increase the cross section much more, producing the improved agreement. The shapes of the σ_{\parallel} and σ_{\perp} angular distributions provide a sensitive test of these cancellations. In Fig. 27 the differences between the data and the calculation are most pronounced at the peak of the Δ . This, along with the incorrect energy dependence for σ_{\parallel} suggest that the source of the remaining discrepancy may lie in the treatment of the Δ .

To avoid double-counting in Ref. [39], a renormalization is made by subtracting the $N\Delta$ box diagram at the photodisintegration threshold. This restores the approximate phase equivalence of the potential at low energies when the Δ degree of freedom is explicitly included. To insure that the Δ is treated correctly at resonance energies, the $M_{1+}(3/2)$ multiple of pion photoproduction is fit to determine the complex, energy-dependent $G_{\Delta N}^{M1}(E)$ coupling. However, the off-shell extrapolation for this empirical information and the character of the smaller partial waves both depend on the particular choice of model used in this fitting procedure. In their multipole fits, Whisnant *et al.*, find that relative sizes of the $M2(^3F_3)$ and $M2(^3P_2)$ multipoles (or other small magnetic

terms) compared to the $M1(^1D_2)$ multipole determines the presence of the “dip.” In the coupled-channel calculation, this distribution of strength and its energy dependence is determined, in part, by the fit near the peak of the Δ , its off-shell extrapolation, and the box-renormalization. The other major ingredient is the inclusion of MEC’s. Now that a more realistic treatment of the MEC’s is included, it may be that the discrepancies in the energy dependence near the peak of the Δ are due to problems in the Δ sector. This suspicion is reinforced by the observation that the agreement with the unpolarized cross section improves at energies well above or below the peak of the Δ [5,39].

IV. CONCLUSION

The photodisintegration of deuterium has been measured from below pion threshold to above the Δ resonance with linearly polarized light. The combined $L1/L3$ data set provides a precise, simultaneous measurement of the polarization-dependent and independent cross section throughout the energy region. The unpolarized angular distributions and integrated cross sections agree well with previous work. The published asymmetries are also in substantial agreement although the older data show more scatter than the present work. There is no measurement of the polarization dependent cross sections with which to compare these data.

Having absolute cross sections for linearly polarized light with the polarization both parallel and perpendicular to the reaction plane throughout a region spanning the peak of the Δ , potentially provides a significant constraint on theoretical models. A quantitative analysis of the data is hampered by the current state of coupled-channels calculations. The recent calculations of Schwamb *et al.* find a marked improvement in the agreement with the inclusion of retardation effects in the meson exchange currents. Yet, significant discrepancies with σ_{\perp} still remain which we speculate may be due to an

inadequate treatment of the Δ . Thus, it comes as no surprise that before detailed information on the NN interaction can be extracted from the data in the resonance region, an accurate picture of the $N\Delta$ interaction is also required. Double polarization experiments are now in preparation at LEGS which will provide sensitive new tests of the NN and $N\Delta$ models.

ACKNOWLEDGMENTS

Finally, we wish to acknowledge our collaborator Giovanni Matone. It was he who originally promoted the pro-

gram of deuteron photodisintegration experiments at LEGS. He will be sorely missed. We would also like to thank E. Cima, A. Kuczewski, F. Lincoln, and E. Turri for their help during the running of these experiments. We are grateful for many very useful discussions with Dr. H. Arenhövel, Dr. T.-S. H. Lee, Dr. M. Schwamb, and Dr. P. Wilhelm, and we thank Dr. D. Dowell for his stimulating assistance with Poisson distributions. The LEGS Collaboration was supported by the U.S. Department of Energy under Contract No. DE-AC02-76CH00016, the National Science Foundation, and the Istituto Nazionale di Fisica Nucleare, Italy.

-
- [1] K. Garrow, Ph.D. thesis, Queens University; (private communication); Saskatoon experiment, 1991.
- [2] P. A. Wallace, Ph.D. thesis, University of Glasgow; (private communication); Mainz experiment, 1989.
- [3] P. Levi Sandri *et al.*, Phys. Rev. C **39**, 1701 (1989).
- [4] J. Arends, H. J. Gassen, A. Hegerath, B. Meching, G. Nöldeke, P. Prenzel, T. Reichelt, and A. Voswinkel, Nucl. Phys. **A412**, 50 (1984).
- [5] R. Crawford *et al.*, Nucl. Phys. **A603**, 303 (1996).
- [6] G. S. Chulick *et al.*, Phys. Rev. C **37**, 1549 (1988).
- [7] W. Leidemann and H. Arenhövel, Nucl. Phys. **A465**, 573 (1987).
- [8] M. T. Peña, H. Garcilazo, U. Oelfke, and P. U. Sauer, Phys. Rev. C **45**, 1487 (1992).
- [9] The LEGS Collaboration, G. S. Blanpied *et al.*, Phys. Rev. Lett. **67**, 1206 (1991).
- [10] The LEGS Collaboration, G. Blanpied *et al.*, Phys. Rev. C **52**, R455 (1995).
- [11] LEGS Data Release #L1-3.0, March/94, available via <http://www.legs.bnl.gov/~legs/>.
- [12] B. M. Preedom *et al.*, Nucl. Instrum. Methods **133**, 311 (1976).
- [13] C. A. Baker *et al.*, Nucl. Instrum. Methods **71**, 117 (1969).
- [14] J. N. Palmiere *et al.*, Nucl. Instrum. Methods **76**, 55 (1969).
- [15] E. DeSanctis *et al.*, Phys. Rev. C **34**, 413 (1986).
- [16] A. M. Sandorfi, M. J. LeVine, C. E. Thorn, G. Giordano, G. Matone, and C. Scharf, IEEE Trans. Nucl. Sci. **30**, 3083 (1983).
- [17] C. E. Thorn, G. Giordano, O. C. Kistner, G. Matone, A. M. Sandorfi, C. Schaerf, and C. S. Whisnant, Nucl. Instrum. Methods Phys. Res. A **285**, 447 (1989).
- [18] O. Klein *et al.*, Z. Phys. **52**, 853 (1928).
- [19] R. Machleidt, Adv. Nucl. Phys. **19**, 189 (1989).
- [20] R. D. Amado, Phys. Rev. C **19**, 1473 (1979).
- [21] J. L. Friar, Phys. Rev. C **20**, 325 (1979).
- [22] B. Desplanques, Phys. Lett. B **203**, 200 (1988).
- [23] The Scattering Analysis Interactive Dial-in (SAID) program, available by TELNET to VTINTE.PHYS.VT.EDU {physics, quantum}.
- [24] R. Dubois *et al.*, Nucl. Phys. **A377**, 544 (1982).
- [25] K.-M. Schmitt and H. Arenhövel (private communication). The calculations presented here are extensions of those presented in Few-Body Syst. **7**, 95 (1989).
- [26] P. Wilhelm, W. Leidemann, and H. Arenhövel, Few-Body Syst. **3**, 111 (1988).
- [27] M. Lacombe, B. Loiseau, J. M. Richard, R. Vinh Mau, J. Côte, P. Pirès, and R. de Tourreil, Phys. Rev. C **21**, 861 (1980).
- [28] P. Wilhelm and H. Arenhövel, Phys. Lett. B **318**, 410 (1993).
- [29] H. Tanabe and K. Ohta, Phys. Rev. C **40**, 1905 (1989).
- [30] T.-S. H. Lee, *5th Workshop on Perspectives in Nuclear Physics at Intermediate Energies*, ICTP, Trieste, Italy, 1991 (World Scientific, Singapore, 1992).
- [31] F. F. Liu, Phys. Rev. **138**, B1443 (1965).
- [32] G. Barbiellini, C. Berardini, F. Felicetti, and G. P. Murtas, Phys. Rev. **154**, 988 (1967).
- [33] V. G. Gorbenko, Yu. V. Zhebrovskij, L. Ya. Kolesnikov, A. L. Rubashkin, and P. V. Sorokin, Nucl. Phys. **A381**, 330 (1982).
- [34] F. V. Adamian *et al.*, J. Phys. G **17**, 1189 (1991).
- [35] S. Wartenberg *et al.*, Few-Body Syst. **26**, 213 (1999).
- [36] H. Arenhövel, Nucl. Phys. **A374**, 521c (1982).
- [37] J. M. Laget, Can. J. Phys. **62**, 1046 (1984).
- [38] C. S. Whisnant, W. K. Mize, D. Pomarède, and A. M. Sandorfi, Phys. Rev. C **58**, 289 (1998).
- [39] M. Schwamb, H. Arenhövel, P. Wilhelm, and Th. Wilbois, Phys. Lett. B **420**, 255 (1998); Nucl. Phys. **A631**, 583c (1998); (private communication).